

33 **Abstract/Summary**

34 Myocardial infarction (MI) promotes a range of systemic effects, many of which are
35 unknown. Here, we investigated the alterations associated with MI progression in heart and
36 other metabolically active tissues (liver, skeletal muscle, and adipose) in a mouse model of
37 MI (induced by ligating the left ascending coronary artery) and sham-operated mice. We
38 performed a genome-wide transcriptomic analysis on tissue samples obtained 6- and 24-hours
39 post MI or sham operation. By generating tissue-specific biological networks, we observed:
40 (1) dysregulation in multiple biological processes (including immune system, mitochondrial
41 dysfunction, fatty-acid beta-oxidation, and RNA and protein processing) across multiple
42 tissues post MI; and (2) tissue-specific dysregulation in biological processes in liver and heart
43 post MI. Finally, we validated our findings in two independent MI cohorts. Overall, our
44 integrative analysis highlighted both common and specific biological responses to MI across a
45 range of metabolically active tissues.

46

47 **Keywords**

48 Systems biology; network analysis; whole-body modelling; cardiovascular disease;
49 Myocardial infarction; multi-tissue; metabolically active tissues; liver; adipose; muscle

50

51 **Introduction**

52 Cardiovascular disease (CVD) is the leading cause of death worldwide, accounting for more
53 than 17 million deaths globally in 2016¹. Myocardial infarction (MI) is one of the most
54 common causes of CVD-related death, and is the result of severe coronary artery disease that
55 develops from tapered arteries or chronic blockage of the arteries caused by accumulation of
56 cholesterol or plaque (atherosclerosis). Many behavioral risk factors (including unhealthy
57 diet, physical inactivity, excessive use of alcohol, and tobacco consumption), which are
58 responsible for hypertension, obesity, diabetes, and hyperlipidemia by significantly altering
59 metabolism, are also implicated in MI. These abnormalities are known as the high-risk factors
60 of MI and CVDs in general.

61
62 Systems biology has been used in many studies to reveal the underlying molecular
63 mechanisms of complex human diseases and to answer important biological questions related
64 to the progression, diagnosis and treatment of the diseases. The use of systems biology has
65 aided the discovery of new therapeutic approaches in multiple diseases²⁻⁴ by identifying
66 novel therapeutic agents and repositioning of existing drugs⁵. Systems biology has also been
67 employed in the identification of novel biomarkers, characterization of patients and
68 stratification of heterogenous cancer patients⁶⁻⁸. Specifically, integrated networks (INs)⁸ and
69 co-expression networks (CNs)⁹ have been proven to be robust methods for revealing the key
70 driver of metabolic abnormalities, discovering new therapy strategies, as well as gaining
71 systematic understanding of diseases^{10,11}.

72
73 Previously, multiple studies in individual tissues have been performed and provided new
74 insights into the underlying mechanisms of diseases¹²⁻¹⁵. However, the crosstalk between
75 different tissues and their dysregulation has not been examined in MI and other CVD-related
76 complications¹⁶. Here we performed an integrated analysis of heart and other metabolically
77 active tissues (liver, skeletal muscle and adipose tissue) using a mouse model of MI. We used
78 several systems biology approaches to obtain a systematic picture of the metabolic alterations
79 that occur after an MI (**Figure 1A**), and validated our findings in two independent datasets.

80 **Results**

81 *Differential expression analysis shows a pronounced effect on gene expression 24 h post*

82 **MI**

83 To study global biological alterations and systemic whole-body effects associated with MI,
84 we obtained heart, liver, skeletal muscle, and white adipose tissue from mice 6 h and 24 h
85 after either an MI (induced by ligating the left ascending coronary artery) or a sham operation
86 (as control). Total of 20 mice were used in this study (5 mice in each time and condition
87 combination) (**Figure 1A**). We generated transcriptomics data and identified differentially
88 expressed genes (DEGs) 6 and 24 h post MI and sham operation in all tissues, with the most
89 significant differences occurring after 24 h (**Supplementary File 1, Figure 1B**). Principal
90 component analysis (PCA) showed a close clustering between the control (for both time
91 points) and MI (6 h and 24 h separately) samples for heart tissue but clustering by extraction
92 time points (6 h and 24 h clusters) for the other tissues (**Figure 1 - Figure Supplement 1**).
93 We present the transcriptional changes associated with MI in **Supplementary File 1** and the
94 DEGs (FDR < 5%) using an UpSet plot¹⁷ in **Figure 1C**.

95

96 All tissues showed a more pronounced effect in terms of the number of DEGs 24 h post MI
97 (**Figure 1C**). As expected, the most affected tissue was the heart (393 DEGs at 6 h, 3318
98 DEGs at 24 h, and 318 DEGs were the same at both time points). By contrast, 136, 641 and
99 374 genes were significantly changed in liver, skeletal muscle and adipose tissues 24 h post
100 MI compared to control, respectively. More than 33% of the DEGs that significantly changed
101 in the other tissues also changed in the heart (**Figure 1C**). Interestingly, more than 97% of the
102 shared DEGs between heart and skeletal muscle changed in the same direction, with
103 corresponding numbers of 88% and 64% in adipose and liver, respectively.

104

105 *Functional analysis reveals widespread alterations of mitochondrial, fatty acid, immune,*
106 *and protein and RNA-related biological processes post MI with liver shows contrasting*
107 *trend*

108 We performed gene-set enrichment analysis (GSEA) with KEGG pathways (**Supplementary**
109 **File 2, Figure 1D**) and gene ontology (GO) biological processes (BPs) (**Supplementary File**
110 **3, Figure 2A**) to identify altered biological functions and pathways 24 h after an MI.

111 Mitochondrial functions (specifically, mitochondrial translation, respiratory chain and
112 oxidative phosphorylation) were significantly downregulated in the heart, muscle and adipose
113 tissues but not in the liver. Processes related to oxidative stress were upregulated in the heart
114 and skeletal muscle. Fatty acid beta-oxidation was downregulated in the heart and adipose but
115 upregulated in the liver. Processes and pathways related to immune systems were
116 significantly upregulated in the heart and skeletal muscle but significantly downregulated in
117 liver. Processes associated with protein and RNA processing, ribosome biogenesis and protein
118 targeting endoplasmic reticulum were upregulated in all tissues except liver whereas protein
119 processing in endoplasmic reticulum and RNA transport pathways were upregulated in all
120 tissues.

121 We also observed that liver was showing opposite trends compared to the other tissues in
122 other important functions, such as fatty acid metabolism and immune response. By checking
123 regulation at the gene level, we observed that only 16 DEGs in liver showed opposite
124 regulation compared to the other tissues whereas 97 out of the 136 DEGs in liver were not
125 DEGs in any other tissues (**Supplementary File 4**). Therefore, the differences we observed in
126 liver were mainly due to different DEGs rather than opposite regulation compared to other
127 tissues.

128

129 *Tissue-specific altered biological functions point to specificity of metabolic and signaling*
130 *responses to MI*

131 The functional analysis also indicated that several metabolic pathways (including cholesterol,
132 ascorbate and aldarate, linoleic acid, and sphingolipid metabolism pathways) and signaling
133 pathways (including GnRH, FoxO, cAMP and prolactin signaling pathways) were
134 significantly upregulated in heart 6 h after an MI (**Supplementary File 2, Figure 1 - Figure**
135 **Supplement 2**). We also observed significant down regulation of tryptophan metabolism and
136 upregulation of glycosaminoglycan biosynthesis in heart 24 h after an MI (**Supplementary**
137 **File 2, Figure 1 - Figure Supplement 2**). Processes related to retinol metabolism were
138 upregulated in heart at both timepoints. Pathways that were previously associated with cardiac
139 hypertrophy and cardiac remodeling (e.g. JAK-STAT, MAPK, estrogen, and TNF signaling
140 pathways, and ECM-receptor interaction) were significantly upregulated in heart 6 and 24 h
141 after an MI (**Figure 1 - Figure Supplement 4**).

142
143 Our analysis also indicated significant metabolic differences in adipose tissue 24 h after an MI
144 (**Figure 1 - Figure Supplement 3**). Fructose and mannose metabolism, glyoxylate and
145 dicarboxylate metabolism, glycolysis/gluconeogenesis, and pentose phosphate pathways,
146 glycine, serine and threonine metabolism and pyrimidine metabolism, as well as endocrine
147 systems (e.g. insulin signaling pathway and regulation of lipolysis in adipocytes) were
148 downregulated in adipose tissue.

149 We observed that the PPAR signaling pathway was upregulated whereas glutathione was
150 downregulated in liver 24 h post-infarction (**Figure 1 - Figure Supplement 3**). We found that
151 sphingolipid metabolism and immune-related pathways were upregulated in skeletal muscle
152 24 h post-infarction (**Figure 1 - Figure Supplement 3**).

153

154 ***Reporter metabolite analyses show significant alterations in fatty acid, amino acid, retinol,***
155 ***and estrogen metabolism post MI***

156 To predict the effect of the transcriptional changes on metabolism, we performed reporter
157 metabolite analyses (**Supplementary File 5**) using the gene-to-metabolites mapping from the
158 Mouse Metabolic Reaction database¹⁸; results in each tissue 24 h after MI are shown in
159 **Figure 2B**. In agreement with our analyses above, reporter metabolites related to oxidative
160 phosphorylation, such as ubiquinol, ubiquinone, NADH and NAD⁺, were downregulated in
161 all tissues except liver. Moreover, linolenoyl-CoA, acetyl CoA, and several other fatty acyl-
162 CoA-related metabolites were downregulated in heart and adipose tissue but upregulated in
163 liver. We also found that several 5-S-glutathionyl metabolite forms, known to be related to
164 phenylalanine, tyrosine and tryptophan biosynthesis, were downregulated in heart, liver and
165 skeletal muscle. The same pattern of downregulation was also observed for metabolites
166 related to estrogen metabolism, specifically metabolites related to oestrone and its glutathione
167 conjugate derivative. Moreover, 12-keto-LTB₄ and 12-oxo-c-LTB₃, related to leukotriene
168 metabolism, and hepxilin A₃, an arachidonic acid, were also found to be downregulated in
169 heart, liver, and skeletal muscle.

170
171 The liver showed the highest alteration in reporter metabolites, which is attributed to its role
172 as one of the most metabolically active tissues. We found that several reporter metabolites
173 related to retinol metabolism, namely retinal, retinol, retinoate, and all-trans-18-
174 hydroxyretinoic acid, were significantly downregulated only in liver tissue. Retinol
175 metabolism has been previously associated with MI^{19,20}.

176
177 ***Network analyses unveil universal and tissue-specific clusters and mechanisms post MI***

178 The use of co-expression network (CN) analyses can assist in elucidating the functional
179 relationships between genes in a specific cell and tissue⁹. Here, we performed CN analysis to
180 reveal the functional relationship between the DEGs by generating tissue-specific CNs and
181 selected highly connected genes (the top 5% positively correlated genes that fulfilled FDR <
182 0.05) (**Table 1**). To better define the structure of the networks, we used the Leiden clustering
183 algorithm²¹ by maximizing the modularity scores (**Figure 3A-D**) and selected the clusters
184 that include more than 30 genes. Next, we superimposed DEGs 24 h post-infarction onto the
185 network (**Supplementary File 1**) and identified the components of the clusters that were

186 affected by an MI. We also used functional analysis with GO BP and KEGG pathways to
187 understand the specific functions associated with each cluster by using the Enrichr algorithm
188 (FDR < 0.05)^{22,23}. We summarized the GO BP terms with Revigo (**Supplementary File 6**)²⁴
189 and checked the average clustering coefficient to define the centrality of each cluster
190 (**Supplementary File 6**)⁹. Among the clusters, we identified the key clusters as those with
191 the highest average clustering coefficient, allowing us to identify sets of genes whose time-
192 dependent coordinated changes showed the strongest relationships.

193

194 Interestingly, key clusters contained genes with similar functionalities including RNA
195 processing, transports, and RNA metabolic processes in all tissue-specific CNs
196 (**Supplementary File 6**). In addition, we found that the majority of the DEGs associated with
197 those clusters were significantly upregulated. These observations strengthen the findings of
198 the functional analysis above (**Figure 2A**) and further highlight how embryonically distinct
199 tissues display similar functional responses to MI, with the most highly connected groups of
200 genes preserved between different tissues (**Supplementary File 6, Figure 3E**).

201

202 *Community detection reveals tissue-specific clusters post MI*

203 We investigated the tissue specificity of each cluster by performing enrichment analysis with
204 data from the Mouse Gene Atlas²⁵, which involved counting the number of tissue-specific
205 genes.

206

207 The heart network showed the highest number of tissue-specific genes in cluster Heart-3 (302
208 genes). Based on DEG analysis, we found that 522 genes were downregulated and 192 genes
209 were upregulated in the cluster. The enriched GO BP terms in the cluster were mitochondrial
210 transport, protein processing and respiratory chain, cardiac muscle cell action potential,
211 response to muscle stretch, and heart contraction (**Figure 3F**). We observed that the results of
212 the KEGG pathway enrichment analysis were consistent with those obtained from GO BP
213 analysis (**Supplementary File 6**).

214

215 In the liver network, cluster Liver-2 showed the highest tissue specificity (479 genes). In this
216 cluster, we found that 15 genes were significantly downregulated and 17 genes were
217 significantly upregulated. Based on GO BP enrichment analysis, the genes in this cluster were
218 associated with cholesterol metabolism and homeostasis, lipid transport, glutathione

219 metabolism, lipoprotein metabolism, and glucose 6-phosphate metabolism (**Supplementary**
220 **File 6**). KEGG enrichment analysis also showed that the genes in the cluster were related to
221 retinol, carbohydrate, lipid and amino-acid metabolism (**Supplementary File 6**).

222

223 The muscle network had two clusters with high tissue specificity: cluster Muscle-4 (276
224 genes) and Muscle-5 (143 genes). Muscle-4 showed association with GO BP terms such as
225 mitochondrial transport, protein processing and respiratory chain, response to muscle stretch,
226 and muscle contraction (**Supplementary File 6**). In contrast, the KEGG pathway in this
227 cluster showed relation to glycolysis/glucogenesis, propanoate metabolism, glyoxylate and
228 dicarboxylate metabolism, and several signaling pathways (e.g. oxytocin, glucagon, cGMP-
229 PKG and HIF-1) (**Supplementary File 6**). Muscle-5 was enriched in GO BP terms associated
230 with protein dephosphorylation, muscle contraction and intracellular protein transport
231 (**Supplementary File 6**). We also found that insulin, MAPK and Wnt signaling pathways
232 were associated to Muscle-5 from the KEGG enrichment analysis (**Supplementary File 6**).

233

234 The adipose tissue network showed tissue specificity in cluster Adipose-2 (33 genes), which
235 is associated with GO BP processes including mRNA processing, regulation of mitotic cell
236 cycle phase, ribosome biogenesis, and viral processes (**Supplementary File 6**). We observed
237 that the results of the KEGG pathway enrichment analysis were consistent with those
238 obtained from GO BP analysis, with additional associations with multiple signaling and
239 regulatory pathways (**Supplementary File 6**).

240

241 *Tissue-specific clusters show important tissue-specific changes post MI*

242 To understand the specific behavior of each tissue, we further studied the tissue-specific
243 clusters in the CNs (**Figure 4A**). Heart specific cluster, Heart-3, was driven by several central
244 genes including *Pln*, *Pde4b*, and *Atp2a2* (related to regulation of cardiac muscle contraction)
245 and *Pdhal* and *Vdac1* (related to mitochondrial functions). These genes were also found to be
246 significantly differentially expressed in heart 24 hours post MI (**Supplementary File 1**).

247 Genes in the heart-specific cluster were related to multiple other processes/pathways, e.g.
248 oxytocin signaling pathway, and several metabolic pathways (glycogen, inositol phosphate
249 and purine) (**Supplementary File 6**).

250

251 Mitochondrial dysfunction in the heart leads to disturbance of energy (ATP) production^{26,27}
252 and, in the presence of oxygen, to accumulation of reactive oxygen species (ROS), which can
253 cause oxidative stress. *Vdac1*, a key gene for regulation of mitochondria function and one of
254 the central genes in the heart-specific cluster (see above), is significantly downregulated in MI
255²⁸. *Vdac1* is located in the outer mitochondrial membrane and is involved directly in
256 cardioprotection²⁹ within the cGMP/PKG pathway (**Figure 4 - Figure Supplement 1**). In the
257 same pathway, we also observed down-regulation of the reporter metabolite hydrogen
258 peroxide (**Supplementary File 5**), a ROS that is related to cardioprotection^{29,30}. We also
259 observed downregulation of *Pdha1*, which is known to have a substantial role in both the
260 HIF-1 signaling pathway and the pyruvate metabolism pathway that converts pyruvate to
261 acetyl-CoA in the mitochondria (**Figure 4 - Figure Supplement 2**). Acetyl-CoA is used in
262 the TCA cycle to produce NADH and FADH₂, which are both needed for ATP production
263 and were downregulated in our reporter metabolite analysis of the heart. Our findings are thus
264 consistent with dysfunctional mitochondria and ATP production in the heart in response to an
265 MI. *Pdha1* has been also been linked to the heart sensitivity during to ischemic stress, where
266 its deficiency can compromise AMP-activated protein kinase activation³¹.

267
268 In skeletal muscle and adipose tissue, we found that central genes in their respective tissue-
269 specific clusters related to fatty acid metabolism and lipid metabolism were significantly
270 altered (**Supplementary File 6, Figure 5**). In liver-specific cluster, we found that their central
271 genes were related to fatty-acid beta oxidation (*Cyp4a31*, *Cyp4a32*) and glutathione
272 metabolism (*Gstm3*) (**Supplementary File 6, Figure 5A**). Alterations of fatty acid beta-
273 oxidation and glutathione metabolism have previously been reported in non-alcoholic fatty
274 liver disease, a known risk factor of CVD^{32,33}. Moreover, in liver, we also found that retinol
275 metabolism was uniquely related to genes in the liver-specific cluster, mainly driven by four
276 significantly differentially expressed central genes of the clusters, i.e. *Cyp26a1*, *Cyp4a31*,
277 *Cyp4a32*, and *Hsd17b6* (**Supplementary File 6**). A previous study showed that mortality
278 from CVD in older individuals was accompanied by impaired liver ability to store retinol¹⁹.

279

280 ***Multi-tissue modeling reveals key metabolic pathways affected post MI***

281 To investigate the metabolic responses to MI in and across tissues in the mice, we constructed
282 a multi-tissue genome-scale metabolic model. The model consisted of five tissue-specific
283 genome scale metabolic models, namely heart, liver, skeletal muscle, adipose, and small

284 intestine. The small intestine model (for which we do not have transcriptomic data) was added
285 to include ingestion and conversion of dietary nutrients into chylomicrons, which are directly
286 secreted into blood and transport lipids to other tissues¹⁸. The final mouse multi-tissue model
287 included 19,859 reactions, 13,284 metabolites, 7,116 genes and 41 compartments. We
288 predicted the metabolic fluxes in mice 24 h after an MI or sham operation by integrating the
289 dietary input, tissue-specific resting energy expenditure and transcriptomics data.

290

291 The modeling showed that oxygen uptake, carbon dioxide production and the oxidative
292 phosphorylation pathway in heart, adipose and skeletal muscle were decreased in MI mice, in
293 agreement with the downregulation of oxidative phosphorylation we observed in these tissues
294 (**Supplementary File 7**). By contrast, liver showed slightly increased oxygen uptake, which
295 might be due to the slightly (not statistically significant) upregulated oxidative
296 phosphorylation (**Supplementary File 7**). These findings indicate that the changes in oxygen
297 and carbon dioxide fluxes and the oxidative phosphorylation pathway could serve as a
298 positive control for predicting the changes due to MI in the fluxes.

299

300 Next, we investigated the tissue-specific metabolic flux changes in the same model
301 (**Supplementary File 7**). We found that the pentose phosphate pathway was upregulated in
302 heart 24 hours post MI, consistent with upregulated glucose metabolism after an MI. Elevated
303 glycolysis could allow the heart to rapidly generate energy under stress conditions, and the
304 enhanced pentose phosphate pathway could increase the NADPH level, which could help
305 maintain the level of reduced glutathione in heart³⁴. In addition, we observed an increase
306 uptake of alpha-ketoglutarate (AKG) of heart 24h after MI. It has been reported that
307 supplementation of AKG could prevent heart from ischaemic injury³⁵, and the increased
308 uptake of AKG we observed after MI might be a natural protective metabolic response to MI.
309 Moreover, we found there is a net lactate metabolic flux coming from liver to heart in the MI
310 group. The influx of lactate has been reported to be positively correlated with the fraction of
311 regional ejection of heart³⁶ and this net flux not only agrees well with the previous report but
312 also additionally suggested the source of the lactate. We also found that adipose tissue
313 secreted more ketone bodies, including acetoacetate and butyrate, into plasma; the plasma
314 level of ketone bodies has been reported as a stress marker in acute MI³⁷. Notably, relatively
315 small metabolic changes were found in liver and skeletal muscle, which is probably due to the
316 small number of transcriptomic changes in metabolic pathways in these tissues.

317

318 ***Validating our findings with publicly available datasets***

319 We validated our observations in heart tissue in two independent cohorts of bulk RNA-seq
320 data from mouse heart (**Supplementary File 8**). We filtered both validation cohorts to get and
321 analyzed only 24 hours post-MI data. We found that there were 2169 DEGs from our heart 24
322 h post MI data were validated in at least one of the independent cohorts (959 DEGs validated
323 in both) (**Figure 6A**). We also found that 109 out of the 123 most connected genes in our
324 heart-specific cluster were also significantly differentially expressed in at least one of the
325 independent cohorts (81 in both). By performing functional analysis of the validation cohorts,
326 we found that ~61% of GO BP and 84% of KEGG pathways identified in our analysis of the
327 heart were also present in at least one of the validation cohorts 24 h after infarction (**Figure**
328 **6B-C**). In both cohorts, we observed downregulation of mitochondrial functions and fatty acid
329 metabolism processes. We also observed upregulation of processes and pathways related to
330 retinol metabolism and inflammatory response in both validation cohorts.

331

332 ***Identification of driver genes in MI***

333 We observed that *Flnc*, *Lgals3*, *Prkaca* and *Pprc1* showed important role to MI. These genes
334 were 4 of 16 genes that were DEGs in at least three tissues and validated in both validation
335 cohorts (**Supplementary File 9**). *Flnc*, *Lgals3* and *Pprc1* were upregulated in heart, skeletal
336 muscle, and adipose, whereas *Prkaca* was downregulated in these three tissues. We further
337 retrieved their neighbors at each tissue specific CNs, showed their regulations from
338 differential expression results, and performed functional analysis in **Supplementary File 9**.

339

340 *Flnc*, which encodes filamin-C, was part of heart and skeletal muscle-specific CN cluster
341 (**Figure S4**). Its neighbor genes were found to be significantly (FDR < 0.05) associated to
342 several functions, including TCA cycle, pyruvate metabolism, glycolysis pathway, and
343 involved in mitochondrial functions. Specifically, they were related to heart-specific
344 processes in heart, VEGF signaling pathway in muscle, carbohydrate metabolism in adipose,
345 and to MAPK signaling pathway and muscle contraction in heart and muscle.

346

347 *Lgals3* (encodes galectin-3) and *Prkaca* were among the most central genes in central clusters
348 (**Supplementary File 6**). The neighbors of *Lgals3* were significantly related to cell cycle and
349 protein digestion and absorption pathway in all tissues, and to RNA and mRNA related-
350 processes in muscle and adipose tissue. The neighbors of *Prkaca* were related to insulin

351 signaling pathway in heart and adipose, and several mitochondrial functions in adipose. *Pprc1*
352 was part of most central clusters in heart and adipose tissue CN, and its neighbors were
353 related to ribosomal RNA processing and ribosome biogenesis.
354

355 **Discussion**

356 CVD has a complex etiology and is responsible for a range of systemic effects, hindering our
357 understanding of its consequences on different tissues. Here, we took advantage of the
358 technological advances in high-throughput RNA-seq and applied integrative network analyses
359 to comprehensively explore the underlying biological effects of MI. Specifically, we
360 generated RNA-seq data from heart, liver, skeletal muscle and adipose tissue obtained from
361 mice 6 and 24 h after an MI or sham operation. We used transcriptomics data analyses
362 (differential expression, functional analysis, and reporter metabolites analysis) to determine
363 the systemic effects of the MI across multiple tissues. Moreover, we performed CN analyses
364 to pinpoint important key and tissue-specific clusters in each tissue, and identified the key
365 genes in each cluster. Finally, we used a whole-body modelling approach to identify the
366 crosstalk between tissues and reveal the global metabolic alterations, before finally validating
367 our findings with publicly available independent MI cohorts.

368

369 Based on our analyses, we observed downregulation of heart-specific functions and
370 upregulation of lipid metabolism and inflammatory response in heart, muscle, and adipose
371 tissue after an MI (**Figure 4B**). Liver showed a distinct response with respect to the other
372 three tissues, including downregulation of inflammatory response. We observed that fatty acid
373 metabolism was downregulated in heart and adipose tissue, whereas fatty acid beta-oxidation
374 was upregulated and glutathione metabolism was downregulated in liver. We also observed
375 upregulation of oxidative stress in heart and skeletal muscle. We also observed
376 downregulation of mitochondrial functions in heart, muscle, and adipose tissue. Furthermore,
377 we found upregulation of retinol metabolism in heart and downregulation of retinol
378 metabolites in liver (**Figure 4B**).

379

380 We hypothesized that downregulation of fatty acid metabolism from adipose tissue was due to
381 exchange of fatty acids with other tissues (liver and muscle) (**Figure 4B**). We also observed
382 the flow of retinol from liver to heart during MI, consistent with previous reports²⁰. These
383 MI-associated alterations lead to dysfunctional mitochondria and decreased energy
384 production, especially in heart and skeletal muscle.

385

386 We also validated our results with publicly available MI datasets generated in separate
387 independent studies. The validation results strengthened our findings on the altered
388 functions/pathways and the important heart-specific genes after an MI.

389

390 Importantly, our analyses of gene clusters highlighted multiple key genes in the response to
391 MI in different tissues. Specifically, we observed that *Flnc*, *Prkaca*, *Lgals3*, and *Pprc1*
392 showed important responses in heart, skeletal muscle, and adipose tissue. *Flnc* is involved in
393 actin cytoskeleton organization in heart and skeletal muscle, and previous studies have shown
394 that this gene has critical role in CVD^{38,39}. Similarly, *Prkaca*, an important metabolic gene,
395 has also been shown to play an important function during CVD⁴⁰⁻⁴². *Lgals3*, related to acute
396 inflammation response, has been studied intensively in recent years as a key gene in CVD,
397 and as a potential CVD therapy target^{43,44}. Lastly, *Pprc1*, as important regulator of
398 mitochondrial biogenesis, has not been explored for its direct relationship with CVD;
399 however, mitochondrial biogenesis appears to be an important response to CVD⁴⁵⁻⁴⁷.

400

401 We recognized several limitations to be noted on this research. First, only transcriptomic data
402 was analyzed in this research, hence the sensitivity might be limited especially for short
403 timepoint, e.g. 6 hours after MI. Second, we focused our analysis in this research only on
404 protein-coding genes. Third, to explore more about the shift in metabolism due to MI, longer
405 timepoints needs to be explored. This opens new opportunities for future research, including
406 analyzing the non-protein-coding gene signatures and longer timepoints.

407

408 In summary, we systematically unveiled the deregulation of biological processes and
409 pathways that resulted from MI in heart, liver, muscle, and adipose tissue by integrating
410 transcriptomic data and the use of biological networks. We also identified the key clusters and
411 central genes using generated tissue-specific CNs. In this study, we demonstrated a strategy to
412 utilize multi-tissue transcriptomic data to identify alteration of biological processes and
413 pathways to systemically explore the effect of a disease.

414

415 **Author Contribution**

416 MK performed the animal experiments, MA performed the computational analysis and
417 analyzed the clinical data together with RB, SD, HT, MU, MC, JW, DE, CZ, AM, and JB

418 coordinated the generation of the clinical data. MA, MK, AM and JB wrote the paper and all
419 authors were involved in editing the paper.

420

421 **Acknowledgements**

422 This work was financially supported by the Knut and Alice Wallenberg Foundation, Swedish
423 Research Foundation and Swedish Heart-Lung Foundation.

424

425 **Conflict of Interest**

426 JW, MC, DE are employees at AstraZeneca. The other authors declare no conflict of interest.

427

| Key Resources Table | | | | |
|---|---|----------------------------|--------------------|----------------------------------|
| Reagent type (species) or resource | Designation | Source or reference | Identifiers | Additional information |
| commercial assay or kit | RNeasy Fibrous Tissue Mini Kit | Qiagen | | Heart and Skeletal Muscle Tissue |
| commercial assay or kit | RNeasy Mini Kit | Qiagen | | Liver Tissue |
| commercial assay or kit | RNeasy Lipid Tissue Mini Kit | Qiagen | | Adipose Tissue |
| commercial assay or kit | cDNA Reverse Transcription Kit | Applied Biosystems | | |
| commercial assay or kit | TaqMan real-time PCR in a ViiA™ 7 system | Applied Biosystems | | |
| commercial assay or kit | NovaSeq6000 | Illumina | | |
| software, algorithm | NovaSeq Control Software 1.6.0/RNA v3.4.4 | Illumina | | |
| software, algorithm | CASAVA Software Suite | Illumina | | |
| software, algorithm | Kallisto | | RRID:SCR_016582 | |
| software, | Python 3.7 | Python | RRID:SCR_008394 | |

| | | | | |
|------------------------|----------------------|---|---|--|
| algorithm | | Programmin g Language | | |
| software, algorithm | sklearn | Python Package | RRID:SCR_019053 | |
| software, algorithm | R | R Project for Statistical Computing | RRID:SCR_001905 | |
| software, algorithm | Rpy2 | Python Package | https://rpy2.github.io/ | |
| software, algorithm | DESeq2 | R Package | RRID:SCR_015687 | |
| software, algorithm | PIANO | R Package | RRID:SCR_003200 | |
| software, algorithm | SciPy | Python Package | RRID:SCR_008058 | |
| software, algorithm | Statsmodel | Python Package | RRID:SCR_016074 | |
| software, algorithm | iGraph | Python Package | RRID:SCR_019225 | |
| software, algorithm | Leiden Clustering | Python Package | https://github.com/vtraag/leidenalg | |
| software, algorithm | Matlab | Mathworks | RRID:SCR_001622 | |

429

430 ***Induction of MI***

431 10-week-old male C57Bl/6N mice were fasted for 4 h before induction of myocardial
432 infarction. The mice were then anesthetized with isoflurane, orally intubated, and connected
433 to a small-animal ventilator (SAR-830, Geneq, Montreal, Canada) distributing a mixture of
434 oxygen, air and 2–3% isoflurane. ECG electrodes were placed on the extremities, and cardiac
435 rhythm was monitored during surgery. An incision was made between the 4th and 5th ribs to
436 reveal the upper part of the anterior left ventricle (LV) wall and the lower part of the left
437 atrium. Myocardial infarction was induced by ligating the left anterior descending (LAD)
438 coronary artery immediately after the bifurcation of the left coronary artery 1. The efficacy of
439 the procedure was immediately verified by characteristic ECG changes, and akinesis of the
440 LV anterior wall. After verification of the infarction, the lungs were hyperinflated, positive

441 end-expiratory pressure was applied, and the chest was closed. Sham mice were handled
442 identically (fasted, anesthetized, intubated, and connected to ventilator, and subsequently
443 incised between 4th and 5th ribs), but no ligation of the LAD coronary artery was performed
444 (and thus, no ischemia was induced in these mice). The mice received an intraperitoneal
445 injection of 0.1 ml buprenorphine to relieve postoperative pain and were allowed to recover
446 spontaneously after stopping isoflurane administration. Mice were killed with an overdose of
447 isoflurane 6 h or 24 h after occlusion or sham operation. We collected the left ventricle (the
448 whole left ventricle containing mainly infarcted tissue) of the heart, whereas white adipose
449 tissue (WAT) was collected from the abdomen and musculus soleus was taken as the muscle
450 tissue. Mouse hearts and biopsies from the liver, muscle and WAT were snap-frozen in liquid
451 nitrogen and stored at -80°C until analysis. All mice studies were approved by the local
452 animal ethics committee and conform to the guidelines from Directive 2010/63/EU of the
453 European Parliament on the protection of animals used for scientific purposes.

454

455 *Echocardiography in mice*

456 Echocardiographic examination, using VisualSonics VEVO 2100 system (VisualSonics Inc,
457 Ontario, Canada), which includes an integrated rail system for consistent positioning of the
458 ultrasound probe was performed 6 and 24 h after an MI to determine the size of the MI. We
459 calculated infarct size based on wall motion score index (WMSI) 24 h after myocardial
460 infarction by a 16-segments model on 3 short axis images, as 0 for normal, ½ for reduced wall
461 thickening and excursion in a segment and 1 for no wall thickening and excursion in a
462 segment. WMSI was calculated as the sum of scores divided by the total number of segments.
463 Hair removal gel was applied to isofluorane-anesthetized (1.2%) mice chest to minimize
464 resistance to ultrasonic beam transmission. The mice were then placed on a heating pad and
465 extremities were connected to an ECG. A 55 MHz linear transducer (MS550D) was used for
466 imaging. An optimal parasternal long axis (LAX) cine loop of >1000 frames/s was acquired
467 using the ECG-gated kilohertz visualization technique. Parasternal short axis cine-loops were
468 acquired at 1, 3, and 5 mm below the mitral annulus. Infarct size was calculated based on wall
469 motion score index 6 and 24 hours after myocardial infarction by a 16-segments model on
470 LAX and 3 short axis images view, as 0 for normal, ½ for reduced wall thickening and
471 excursion in a segment and 1 for no wall thickening and excursion in a segment. The data
472 were evaluated using VevoStrain™ software system (VisualSonics Inc, Ontario, Canada).

473

474 ***RNA extraction and sequencing***

475 Total RNA was isolated from snap-frozen tissues using RNeasy Fibrous Tissue Mini Kit
476 (Qiagen) for heart and skeletal muscle, RNeasy Mini Kit (Qiagen) for liver, or RNeasy Lipid
477 Tissue Mini Kit (Qiagen) for adipose tissue. cDNA was synthesized with the high-capacity
478 cDNA Reverse Transcription Kit (Applied Biosystems) and random primers. mRNA
479 expression of genes of interest was analyzed with TaqMan real-time PCR in a ViiA™ 7
480 system (Applied Biosystems). RNA sequencing library were prepared with Illumina RNA-
481 Seq with Poly-A selections. Subsequently, the libraries were sequenced on NovaSeq6000
482 (NovaSeq Control Software 1.6.0/RNA v3.4.4) with a 2x51 setup using ‘NovaSeqXp’
483 workflow in ‘S1’ mode flow cell. The Bcl was converted to FastQ by bcl2fastq_v2.19.1.403
484 from CASAVA software suite (Sanger/phred33/Illumina 1.8+ quality scale).

485

486 ***RNA-sequencing data analysis***

487 The raw RNA-sequencing results were processed using Kallisto⁴⁸ with index file generated
488 from the Ensembl mouse reference genome (Release-96)⁴⁹. The output from Kallisto, both
489 estimated count and TPM (Transcript per kilobase million), were subsequently mapped to gene
490 using the mapping file retrieved from Ensembl BioMart website, by filtering only protein
491 coding genes and transcripts. Genes with mean expression less than 1 TPM in each condition
492 were filtered. For data exploration, we used PCA from sklearn package⁵⁰ in Python 3.7 and
493 used TPM values as the input.

494 Subsequently, we performed differential gene expression analysis using DESeq2⁵¹ package in
495 R. We utilized the capabilities from DESeq2 to normalize the rounded estimated count data
496 and to correct for confounding factors (such as time). To define a gene as differentially
497 expressed (DEGs), a gene has to fulfill a criterion of FDR < 5%. The results of differential
498 expression analysis were then used for functional analysis.

499

500 We checked the tissue specificity of the DEGs in each tissue with the data from Mouse Gene
501 Atlas²⁵. For all the tissue-specific genes, we also checked their human-homolog genes in the
502 human secretome database⁵².

503

504 ***Functional analysis***

505 We performed functional analysis using the R package PIANO⁵³. As the input, we used the
506 fold changes and p-values from the DESeq2, and also GO BP and KEGG pathways gene-set
507 collections from Enrichr^{22,23}, and metabolites from Mouse Metabolic Reaction database¹⁸.
508 To define a process or pathway as significant, we used a cut off of FDR < 5% for the distinct
509 direction of PIANO (both up and down).

510

511 ***Co-expression network generation***

512 We generated the co-expression network by generating gene-gene Spearman correlation ranks
513 within a tissue type, using *spearmanr* function from SciPy⁵⁴ in Python 3.7. Using the same
514 environment, we performed multiple hypothesis testing using Benjamini-Hochberg method
515 from *statsmodels*⁵⁵. Correlation data were filtered with criterion of adjusted p-value < 5%.

516

517 The top 5% of filtered correlation results were then loaded into iGraph module⁵⁶ in Python
518 3.7 as an unweighted network. To find the subnetworks, we employed the Leiden clustering
519 algorithm²¹ with *ModularityVertexPartition* method. Each cluster was analyzed by using
520 Enrichr^{22,23} to get the enriched GO BP and KEGG pathways. Criterion FDR < 0.05 were used
521 to find the significantly enriched terms. Clusters with less than 30 genes were discarded, to be
522 able to get significant functional analysis results. Since GO BP was relatively sparse, we used
523 Revigo²⁴ to summarize the GO BP into a higher level. Revigo was further employed to build
524 a GO BP network. Clustering coefficient was calculated based on the average local clustering
525 coefficient function within iGraph.

526

527 ***Multi-tissue metabolic modeling***

528 We combined tissue-specific models (of heart, liver, muscle, adipose and small intestine)
529 constructed previously¹⁸ in a multi-tissue model by adding an additional compartment
530 representing the plasma, which allows the exchange of metabolites among different tissues.
531 Blocked reactions that could not carry fluxes (and the unused metabolites and genes linked to
532 these reactions) were removed from the models. In addition, the dietary input reactions and
533 constraints were added to the small intestine model to simulate the food intake
534 (**Supplementary File 7**). Specifically, we assumed that the mice weighed 30 g and consumed
535 4.5 g chow diet per day (15 g/100 g body weight) based on a previous study⁵⁷. We also

536 calculated the tissue-specific resting energy expenditures and set them as mandatory
 537 metabolic constraints based on previous studies and resting energy expenditure for other
 538 tissues was incorporated by including a mandatory glucose secretion flux out from the system
 539 with the lower bound calculated based on ATP (**Supplementary File 7**)⁵⁷.

540

541 To simulate the metabolic flux distribution in the sham-operated mice, we set the lipid droplet
 542 accumulation reaction in adipose tissue (m3_Adipose_LD_pool) as the objective function as
 543 we assume the energy additional to the resting energy expenditure will be mostly stored as fat
 544 rather than used by the muscle for physical activities because mice raised in the cages might
 545 have very little exercise. Then, we used parsimonious FBA to calculate the flux distribution.
 546 To simulate the flux distribution after an MI, we calculated an expected flux fold change of
 547 each reaction based on the FDR and expression fold changes of all genes associated with the
 548 reaction, and obtains a flux distribution that is closest to this expected flux distribution while
 549 satisfying the stoichiometric balance and flux constraints of the model. The mathematical
 550 formulation of the method is described as below,

$$\begin{aligned} \text{minimize } Z &= \sum_i |v_i - v_i^{exp}| \\ \text{s. t. } S * v &= 0 \\ lb &\leq v \leq ub \end{aligned}$$

551 where S , v , lb , ub represent the stoichiometric matrix, flux distribution, lower bound and
 552 upper bound of all reactions, respectively. The v_i^{exp} represents the expected flux of i^{th}
 553 reaction which is calculated as follows,

$$v_i^{exp} = v_i^{ref} * \sqrt[m]{\prod_{j=1}^m FC_j}$$

554 where n is the number of gene sets that could independently catalyze the corresponding
 555 reaction, and FC_j represents the expected expression changes of j^{th} gene set which is
 556 calculated below,

$$FC_j = (1 - P_1) * fc_1 + P_1(1 - P_2) * fc_2 + \dots + \prod_{k=1}^{m-1} P_k(1 - P_n) * fc_n$$

557 where m is the number of genes in the i^{th} gene sets, and P_j and fc_j respectively represents the
 558 FDR and fold change of gene expression with j^{th} smallest fold change in this gene set. In this
 559 way, genes with lowest fold change will have a dominating effect within a gene set encoding

560 a protein complex, while the geometric mean of expected fold changes of gene sets encoding
561 different isozymes of this reaction will be used as the final expected flux fold change of this
562 reaction.

563

564 ***Validation of the results***

565 We validated our findings by performing similar steps of RNA sequencing and functional
566 analysis for the publicly available mouse MI datasets GSE104187 and GSE52313^{14,15}.

567

568 ***Data and code availability***

569 All raw RNA-sequencing data generated from this study can be accessed through accession
570 number GSE153485. Codes used during the analysis are available on

571 https://github.com/sysmedicine/ArifEtAll_2020_MultiTissueMI

572 **References**

- 573 1 WHO. *Cardiovascular diseases (CVDs) Fact sheets*, <[https://www.who.int/news-](https://www.who.int/news-room/fact-sheets/detail/cardiovascular-diseases-(cvds))
574 [room/fact-sheets/detail/cardiovascular-diseases-\(cvds\)](https://www.who.int/news-room/fact-sheets/detail/cardiovascular-diseases-(cvds))> (2019).
- 575 2 Mardinoglu, A., Boren, J., Smith, U., Uhlen, M. & Nielsen, J. The employment of
576 systems biology in gastroenterology and hepatology. *Nat. Rev. Gastroenterol. Hepatol*
577 (2017).
- 578 3 Mardinoglu, A. & Nielsen, J. New paradigms for metabolic modeling of human cells.
579 *Current Opinion in Biotechnology* **34**, 91-97 (2015).
- 580 4 Nielsen, J. Systems biology of metabolism: a driver for developing personalized and
581 precision medicine. *Cell metabolism* **25**, 572-579 (2017).
- 582 5 Turanli, B. *et al.* Discovery of therapeutic agents for prostate cancer using genome-
583 scale metabolic modeling and drug repositioning. *EBioMedicine* **42**, 386-396 (2019).
- 584 6 Benfeitas, R. *et al.* Characterization of heterogeneous redox responses in
585 hepatocellular carcinoma patients using network analysis. *EBioMedicine* **40**, 471-487
586 (2019).
- 587 7 Bidkhorji, G. *et al.* Metabolic network-based stratification of hepatocellular carcinoma
588 reveals three distinct tumor subtypes. *Proceedings of the National Academy of*
589 *Sciences* **115**, E11874-E11883 (2018).
- 590 8 Lee, S. *et al.* Integrated network analysis reveals an association between plasma
591 mannose levels and insulin resistance. *Cell metabolism* **24**, 172-184 (2016).
- 592 9 Lee, S. *et al.* Network analyses identify liver-specific targets for treating liver
593 diseases. *Molecular systems biology* **13** (2017).
- 594 10 Bakhtiarizadeh, M. R., Hosseinpour, B., Shahhoseini, M., Korte, A. & Gifani, P.
595 Weighted Gene Co-expression Network Analysis of Endometriosis and Identification
596 of Functional Modules Associated With Its Main Hallmarks. *Frontiers in Genetics* **9**,
597 doi:10.3389/fgene.2018.00453 (2018).
- 598 11 Mukund, K. & Subramaniam, S. Co-expression network approach reveals functional
599 similarities among diseases affecting human skeletal muscle. *Frontiers in physiology*
600 **8**, 980 (2017).
- 601 12 Pedrotty, D. M., Morley, M. P. & Cappola, T. P. Transcriptomic biomarkers of
602 cardiovascular disease. *Progress in cardiovascular diseases* **55**, 64-69 (2012).
- 603 13 Das, S. *et al.* Transcriptomics of cardiac biopsies reveals differences in patients with
604 or without diagnostic parameters for heart failure with preserved ejection fraction.
605 *Scientific reports* **9**, 3179 (2019).
- 606 14 Ounzain, S. *et al.* Genome-wide profiling of the cardiac transcriptome after
607 myocardial infarction identifies novel heart-specific long non-coding RNAs.
608 *European heart journal* **36**, 353-368 (2014).
- 609 15 Williams, A. L. *et al.* HIF1 mediates a switch in pyruvate kinase isoforms after
610 myocardial infarction. *Physiological genomics* **50**, 479-494 (2018).
- 611 16 Priest, C. & Tontonoz, P. Inter-organ cross-talk in metabolic syndrome. *Nature*
612 *Metabolism*, doi:10.1038/s42255-019-0145-5 (2019).

- 613 17 Lex, A., Gehlenborg, N., Strobel, H., Vuillemot, R. & Pfister, H. UpSet: visualization
614 of intersecting sets. *IEEE transactions on visualization and computer graphics* **20**,
615 1983-1992 (2014).
- 616 18 Mardinoglu, A. *et al.* The gut microbiota modulates host amino acid and glutathione
617 metabolism in mice. *Molecular Systems Biology* **11**, 834, doi:10.15252/msb.20156487
618 (2015).
- 619 19 Lima, I., Peres, W., Cruz, S. & Ramalho, A. Association of Ischemic Cardiovascular
620 Disease with Inadequacy of Liver Store of Retinol in Elderly Individuals. *Oxidative*
621 *medicine and cellular longevity* **2018** (2018).
- 622 20 Palace, V. P., Hill, M. F., Khaper, N. & Singal, P. K. Metabolism of vitamin A in the
623 heart increases after a myocardial infarction. *Free Radical Biology and Medicine* **26**,
624 1501-1507 (1999).
- 625 21 Traag, V. A., Waltman, L. & van Eck, N. J. From Louvain to Leiden: guaranteeing
626 well-connected communities. *Scientific reports* **9** (2019).
- 627 22 Chen, E. Y. *et al.* Enrichr: interactive and collaborative HTML5 gene list enrichment
628 analysis tool. *BMC Bioinformatics* **14**, 128, doi:10.1186/1471-2105-14-128 (2013).
- 629 23 Kuleshov, M. V. *et al.* Enrichr: a comprehensive gene set enrichment analysis web
630 server 2016 update. *Nucleic Acids Research* **44**, W90-W97, doi:10.1093/nar/gkw377
631 (2016).
- 632 24 Supek, F., Bošnjak, M., Škunca, N. & Šmuc, T. REVIGO summarizes and visualizes
633 long lists of gene ontology terms. *PloS one* **6**, e21800 (2011).
- 634 25 Su, A. I. *et al.* A gene atlas of the mouse and human protein-encoding transcriptomes.
635 *Proceedings of the National Academy of Sciences of the United States of America* **101**,
636 6062-6067, doi:10.1073/pnas.0400782101 (2004).
- 637 26 Kiyuna, L. A., e Albuquerque, R. P., Chen, C.-H., Mochly-Rosen, D. & Ferreira, J. C.
638 B. Targeting mitochondrial dysfunction and oxidative stress in heart failure:
639 challenges and opportunities. *Free Radical Biology and Medicine* **129**, 155-168
640 (2018).
- 641 27 Palaniyandi, S. S., Qi, X., Yogalingam, G., Ferreira, J. C. B. & Mochly-Rosen, D.
642 Regulation of mitochondrial processes: a target for heart failure. *Drug Discovery*
643 *Today: Disease Mechanisms* **7**, e95-e102 (2010).
- 644 28 Camara, A. K., Zhou, Y., Wen, P.-C., Tajkhorshid, E. & Kwok, W.-M. Mitochondrial
645 VDAC1: a key gatekeeper as potential therapeutic target. *Frontiers in physiology* **8**,
646 460 (2017).
- 647 29 Schwertz, H. *et al.* Myocardial ischemia/reperfusion causes VDAC phosphorylation
648 which is reduced by cardioprotection with a p38 MAP kinase inhibitor.
649 *PROTEOMICS* **7**, 4579-4588, doi:10.1002/pmic.200700734 (2007).
- 650 30 Yada, T. *et al.* Cardioprotective role of endogenous hydrogen peroxide during
651 ischemia-reperfusion injury in canine coronary microcirculation in vivo. *American*
652 *Journal of Physiology-Heart and Circulatory Physiology* **291**, H1138-H1146 (2006).
- 653 31 Sun, W. *et al.* Cardiac-specific deletion of the Pdha1 gene sensitizes heart to
654 toxicological actions of ischemic stress. *Toxicological Sciences* **151**, 193-203 (2016).
- 655 32 Mardinoglu, A. *et al.* Personal model-assisted identification of NAD⁺ and glutathione
656 metabolism as intervention target in NAFLD. *Molecular systems biology* **13** (2017).

- 657 33 Alexander, M. *et al.* Non-alcoholic fatty liver disease and risk of incident acute
658 myocardial infarction and stroke: findings from matched cohort study of 18 million
659 European adults. *bmj* **367**, 15367 (2019).
- 660 34 Tran, D. H. & Wang, Z. V. Glucose Metabolism in Cardiac Hypertrophy and Heart
661 Failure. *Journal of the American Heart Association* **8**, e012673 (2019).
- 662 35 Kjellman, U. *et al.* Alpha-ketoglutarate for myocardial protection in heart surgery.
663 *Lancet* **345**, 552-553, doi:10.1016/s0140-6736(95)90466-2 (1995).
- 664 36 Hattori, R. *et al.* Lactate metabolism in acute myocardial infarction and its relation to
665 regional ventricular performance. *J Am Coll Cardiol* **5**, 1283-1291,
666 doi:10.1016/s0735-1097(85)80338-7 (1985).
- 667 37 Miyamoto, T., Katayama, Y. & Harano, Y. Blood ketone body as a stress marker in
668 acute myocardial infarction. *Nihon Kyukyu Igakukai Zasshi* **10**, 621-622 (1999).
- 669 38 Zhou, Y. *et al.* Loss of Filamin C Is Catastrophic for Heart Function. *Circulation* **141**,
670 869-871 (2020).
- 671 39 Hall, C. L. *et al.* RNA sequencing-based transcriptome profiling of cardiac tissue
672 implicates novel putative disease mechanisms in FLNC-associated arrhythmogenic
673 cardiomyopathy. *International journal of cardiology* **302**, 124-130 (2020).
- 674 40 Diviani, D., Dodge-Kafka, K. L., Li, J. & Kapiloff, M. S. A-kinase anchoring proteins:
675 scaffolding proteins in the heart. *American Journal of Physiology-Heart and*
676 *Circulatory Physiology* **301**, H1742-H1753 (2011).
- 677 41 Turnham, R. E. & Scott, J. D. Protein kinase A catalytic subunit isoform PRKACA;
678 History, function and physiology. *Gene* **577**, 101-108 (2016).
- 679 42 Bers, D. M. Calcium cycling and signaling in cardiac myocytes. *Annu. Rev. Physiol.*
680 **70**, 23-49 (2008).
- 681 43 Zhong, X., Qian, X., Chen, G. & Song, X. The role of galectin-3 in heart failure and
682 cardiovascular disease. *Clinical and Experimental Pharmacology and Physiology* **46**,
683 197-203 (2019).
- 684 44 Suthahar, N. *et al.* Galectin-3 activation and inhibition in heart failure and
685 cardiovascular disease: an update. *Theranostics* **8**, 593 (2018).
- 686 45 Ren, J., Pulakat, L., Whaley-Connell, A. & Sowers, J. R. Mitochondrial biogenesis in
687 the metabolic syndrome and cardiovascular disease. *Journal of molecular medicine*
688 **88**, 993-1001 (2010).
- 689 46 Siasos, G. *et al.* Mitochondria and cardiovascular diseases—from pathophysiology to
690 treatment. *Annals of translational medicine* **6** (2018).
- 691 47 Piantadosi, C. A. & Suliman, H. B. Transcriptional control of mitochondrial
692 biogenesis and its interface with inflammatory processes. *Biochimica et Biophysica*
693 *Acta (BBA)-General Subjects* **1820**, 532-541 (2012).
- 694 48 Bray, N. L., Pimentel, H., Melsted, P. & Pachter, L. Near-optimal probabilistic RNA-
695 seq quantification. *Nature biotechnology* **34**, 525 (2016).
- 696 49 Zerbino, D. R. *et al.* Ensembl 2018. *Nucleic Acids Research* **46**, D754-D761,
697 doi:10.1093/nar/gkx1098 (2017).
- 698 50 Pedregosa, F. *et al.* Scikit-learn: Machine learning in Python. *Journal of machine*
699 *learning research* **12**, 2825-2830 (2011).

700 51 Love, M. I., Huber, W. & Anders, S. Moderated estimation of fold change and
701 dispersion for RNA-seq data with DESeq2. *Genome Biol* **15**, 550,
702 doi:10.1186/s13059-014-0550-8 (2014).

703 52 Uhlén, M. *et al.* The human secretome. *Science Signaling* **12**, eaaz0274,
704 doi:10.1126/scisignal.aaz0274 (2019).

705 53 Våremo, L., Nielsen, J. & Nookaew, I. Enriching the gene set analysis of genome-
706 wide data by incorporating directionality of gene expression and combining statistical
707 hypotheses and methods. *Nucleic Acids Research* **41**, 4378-4391,
708 doi:10.1093/nar/gkt111 (2013).

709 54 Jones, E., Oliphant, T. & Peterson, P. SciPy: Open source scientific tools for Python.
710 (2001).

711 55 Perktold, J., Seabold, S. & Taylor, J. (Oct, 2017).

712 56 Csardi, G. & Nepusz, T. The igraph software package for complex network research.
713 *InterJournal, Complex Systems* **1695**, 1-9, doi:10.5281/zenodo.3630268 (2006).

714 57 Kummitha, C. M., Kalhan, S. C., Saidel, G. M. & Lai, N. Relating tissue/organ energy
715 expenditure to metabolic fluxes in mouse and human: experimental data integrated
716 with mathematical modeling. *Physiological reports* **2** (2014).

717 58 Zhang, C. *et al.* RMetD2: a tool for integration of relative transcriptomics data into
718 Genome-scale metabolic models. *BioRxiv*, 663096 (2019).

719

720

721 **Table**

722 Table 1 Properties of the co-expression network

| Tissue | # of Genes | # of Edges | # of Clusters | Modularity Scores |
|---------|------------|------------|---------------|-------------------|
| Heart | 8793 | 1570898 | 7 | 0.540 |
| Liver | 7760 | 1103589 | 6 | 0.577 |
| Muscle | 8834 | 1660603 | 7 | 0.521 |
| Adipose | 10790 | 2636378 | 8 | 0.495 |

723

724 **Figure Supplements**

725 **Figure 1 - Figure Supplement 1** Data Exploration of the Samples

726 **Figure 1 - Figure Supplement 2** KEGG pathway analysis results for Heart 6- and 24- hours
727 post MI

728 **Figure 1 - Figure Supplement 3** KEGG pathway analysis results for each tissue Liver,
729 Muscle, and Adipose tissue 24 hours post MI.

730 **Figure 1 - Figure Supplement 4** KEGG pathways related to cardiac problems show
731 activation after an MI.

732 **Figure 4 - Figure Supplement 1** cGMP-PKG with overlay data from differential expression
733 and reporter metabolites analysis.

734 **Figure 4 - Figure Supplement 2** HIF-1 signaling pathway with overlay data from differential
735 expression and reporter metabolites analysis.

736 **Supplementary Files**

737 **Supplementary File 1** Differential Expression Analysis Results

- 738 **Supplementary File 2** KEGG Pathways
- 739 **Supplementary File 3** Gene Ontology Biological Processes
- 740 **Supplementary File 4** DEG comparison between Liver and other tissues
- 741 **Supplementary File 5** Reporter Metabolite Analysis
- 742 **Supplementary File 6** Enrichment Analyses of Clusters, Clusters properties
- 743 **Supplementary File 7** Food Intake, Energy Expenditure, and Flux Balance Analysis (FBA)
- 744 of Whole-Body Modeling
- 745 **Supplementary File 8** Validation Result (Differential Expression and Functional Analysis)
- 746 **Supplementary File 9** Detailed Information of 16 Key Genes that are DEGs in at least 3
- 747 tissues and Neighbors and Functional Analysis Results of The Neighbors of 4 key genes

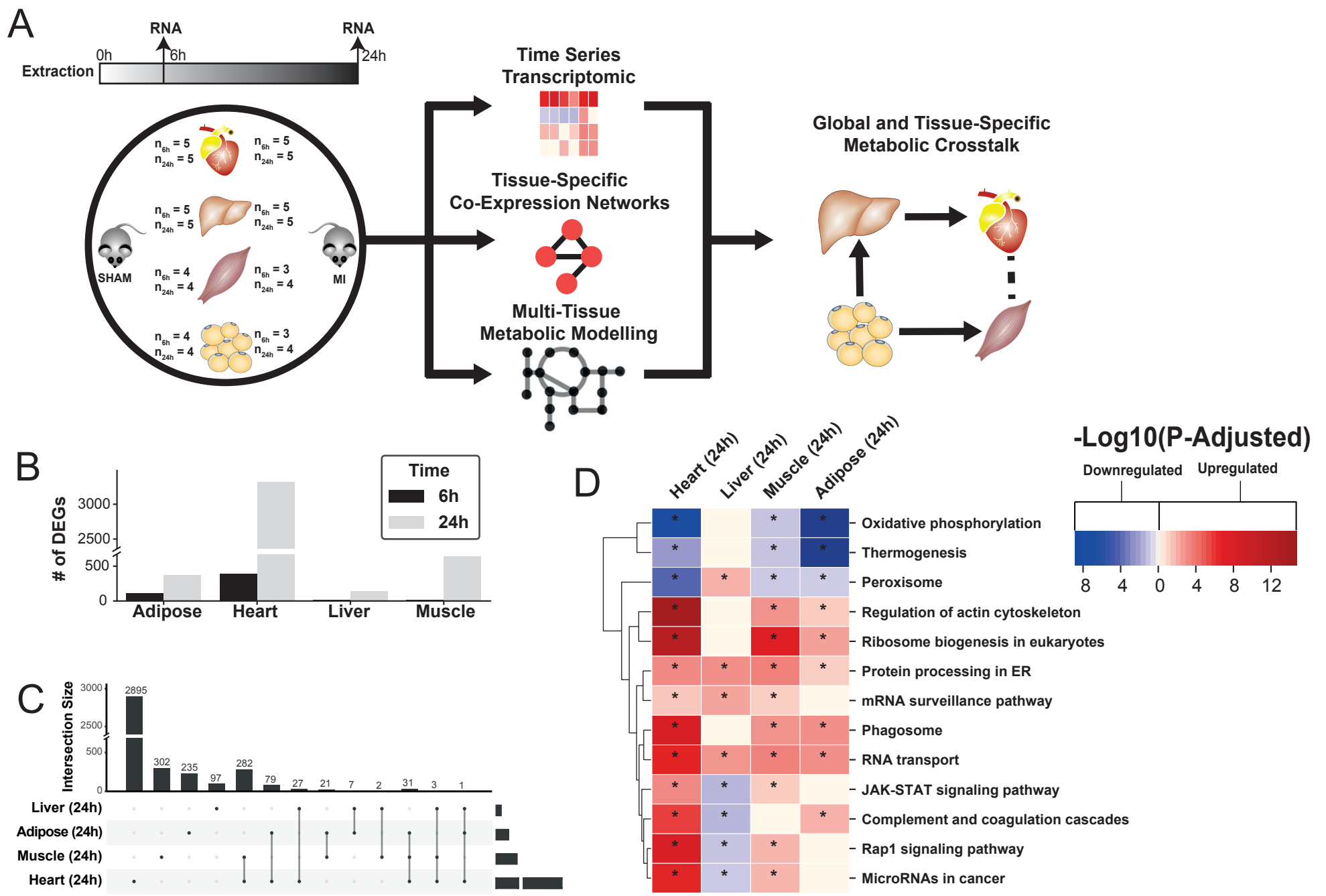


Figure 1 (A) Overview of this study (B) Number of differentially expressed genes for each tissue at each time point. Effect of MI shown to be more pronounced after 24 h. (C) UpSet plot to show intersection between differentially expressed genes (FDR < 5%) in different tissues. The plot showed that each tissue has its specific set of genes that were affected by MI. (D) KEGG pathway analysis (FDR < 0.05 in at least 3 tissues) for 24 hours post MI compared to its control for each tissue. We observed that 141 (5 upregulated) and 125 (14 upregulated) pathways are significantly altered in heart 6 and 24 h after infarction, respectively. For other tissues, we found that 24 (9 upregulated), 61 (54 upregulated) and 48 (15 upregulated) pathways are altered in liver, muscle, and adipose, respectively.

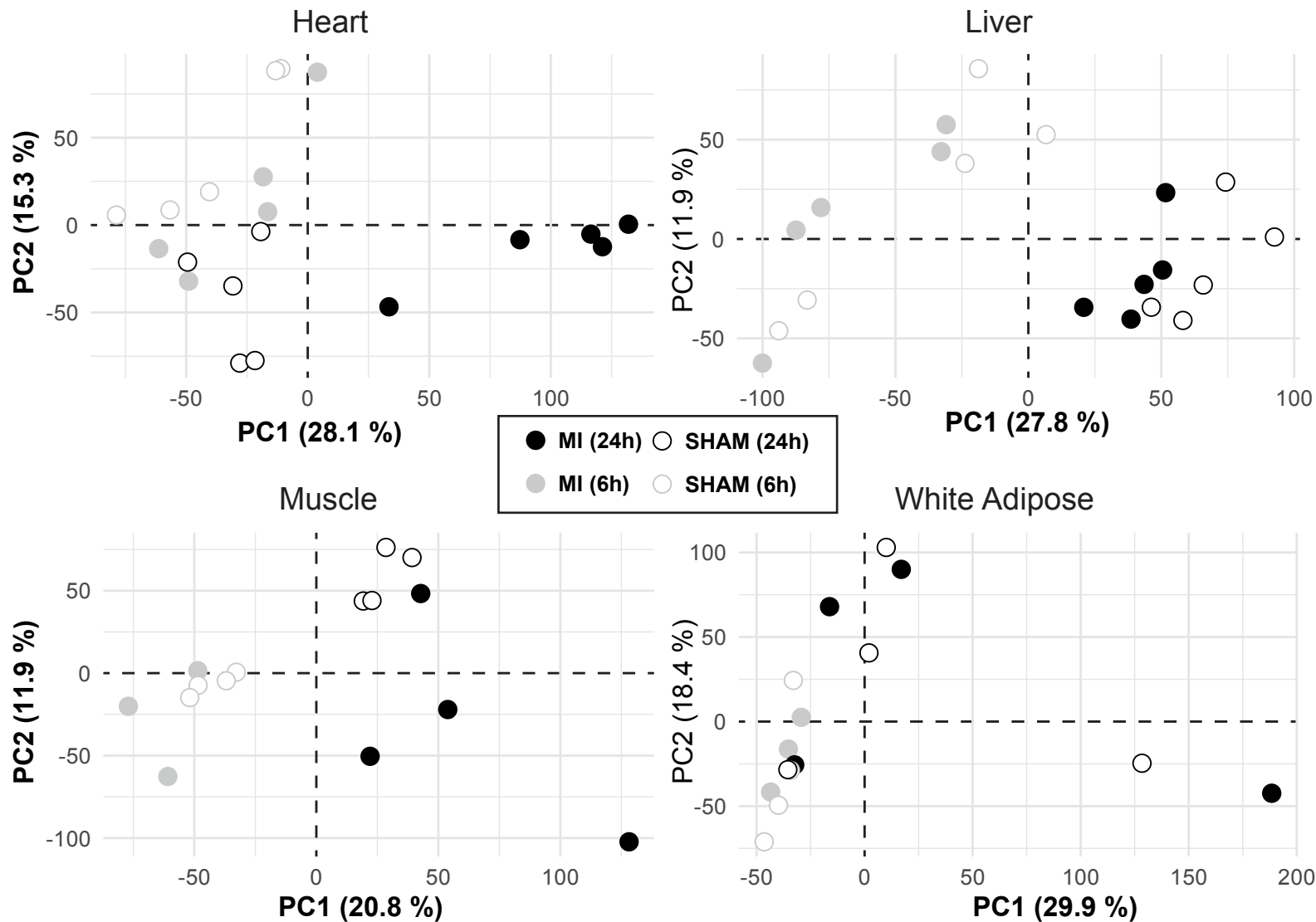
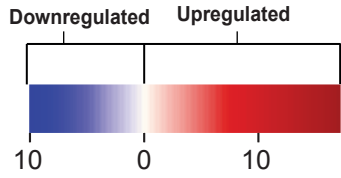


Figure 1 - Figure Supplement 1
Data Exploration of the Samples

PCA plots of each tissue showing data from mice 6 and 24 h after an MI or sham operation. The plot showed that heart was affected the most by the change in conditions and the rest were most affected by time shifts..

-Log10(P-Adjusted)



24h 6h

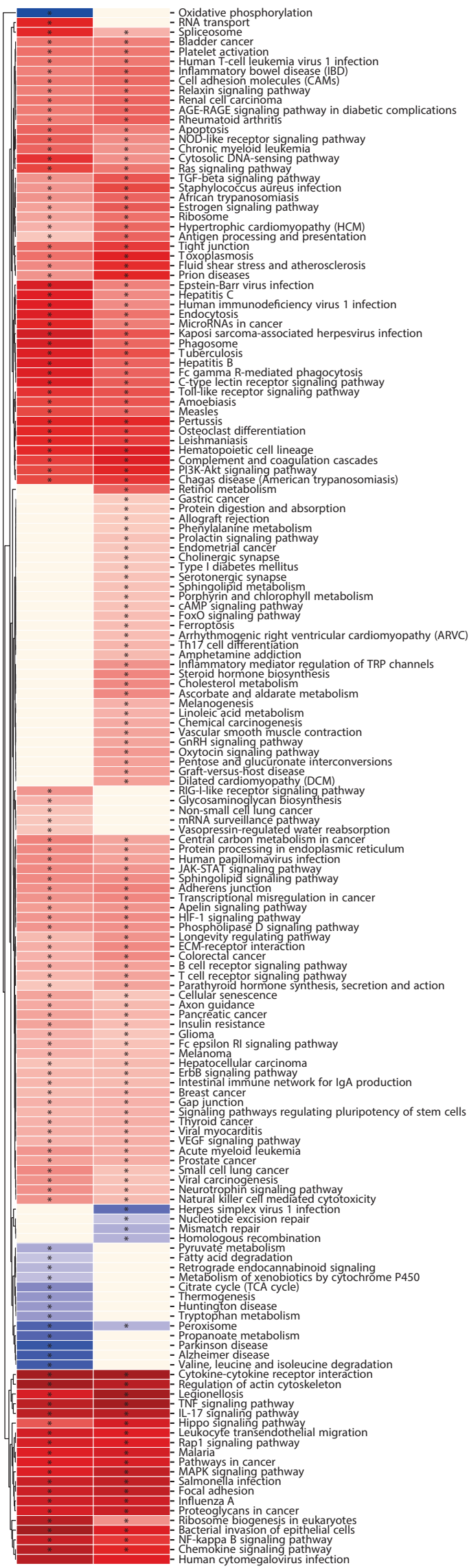
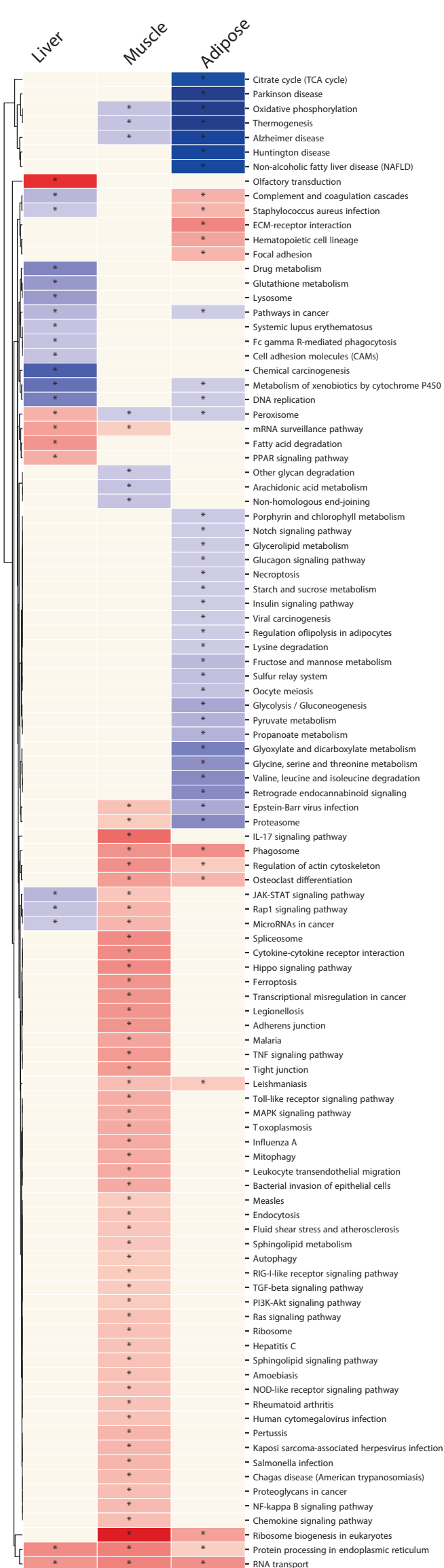


Figure 1 - Figure Supplement 2
KEGG pathway analysis results for Heart 6- and 24- hours post MI



-Log10(P-Adjusted)

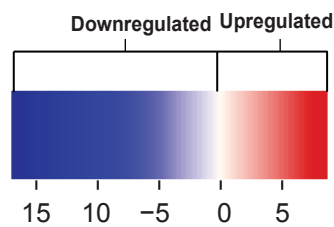


Figure 1 - Figure Supplement 3
KEGG pathway analysis results for each tissue post MI.

Liver, Muscle, and Adipose tissue 24 hours

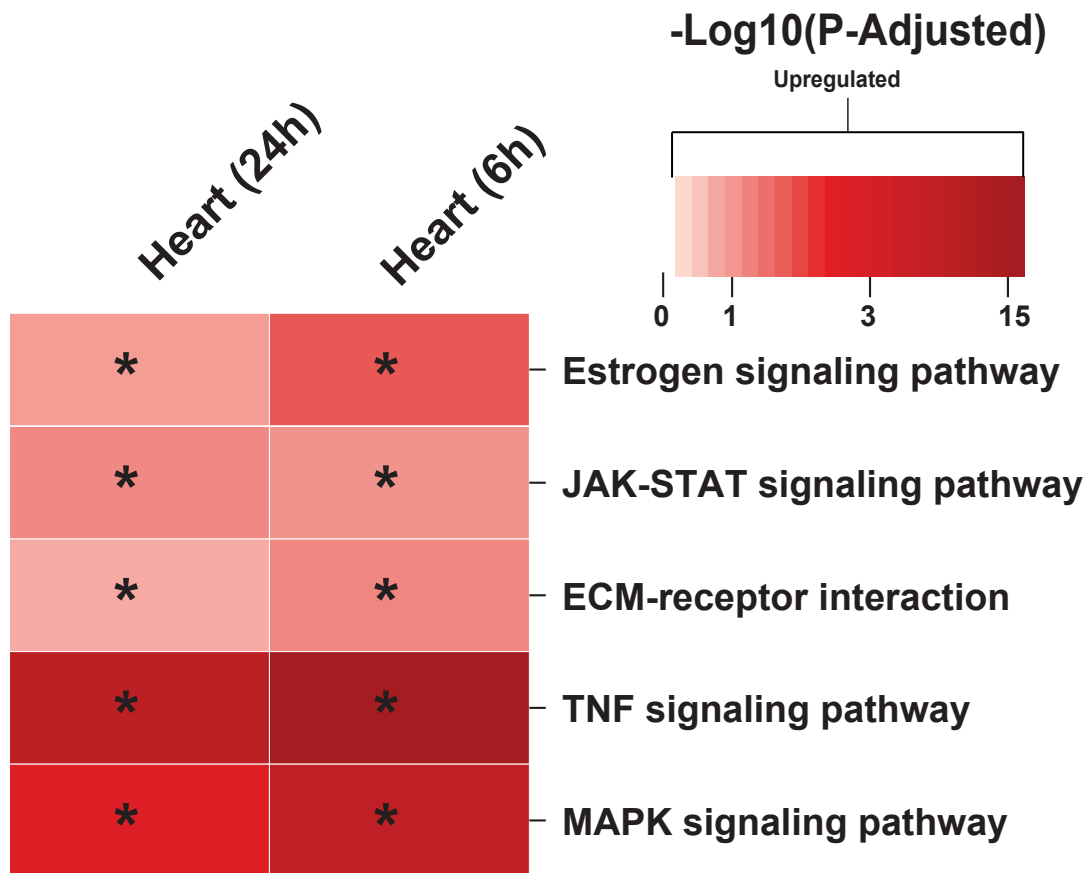


Figure 1 - Figure Supplement 4
KEGG pathways related to cardiac problems show activation after an MI.

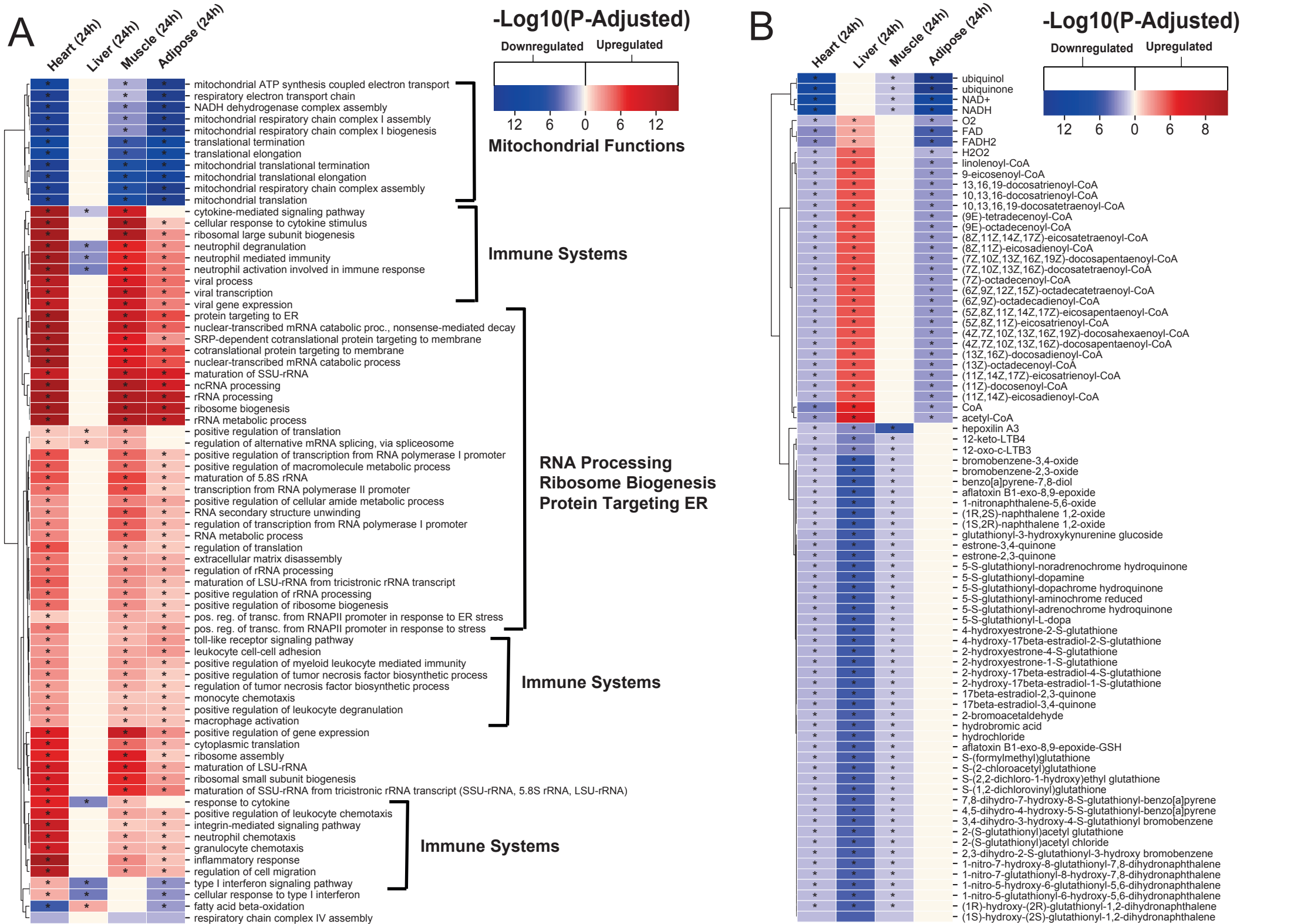
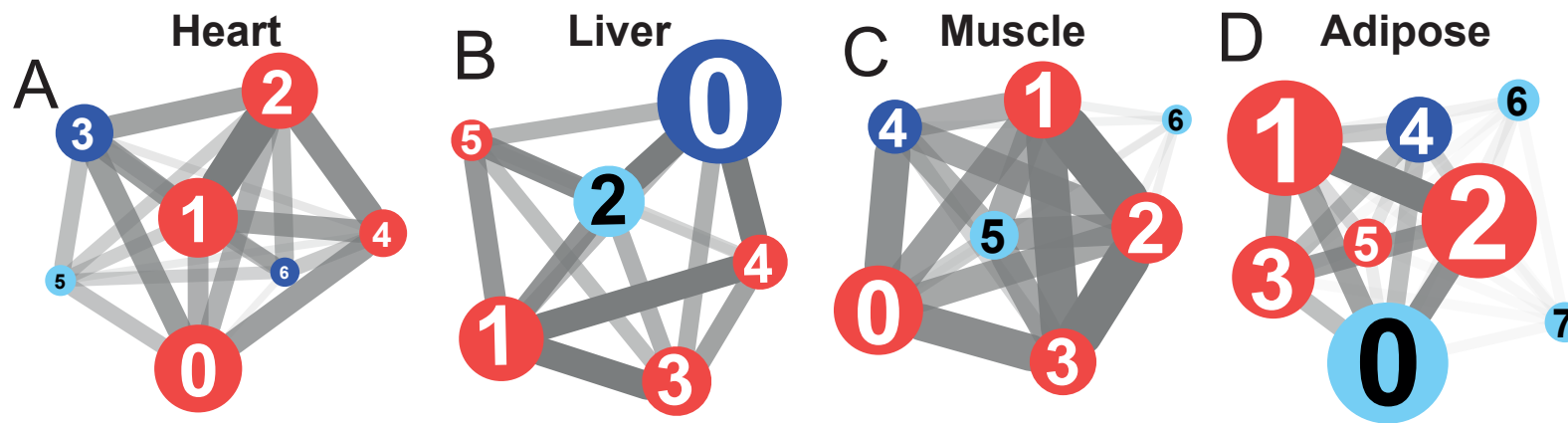


Figure 2 (A) Functional analysis with GO (FDR < 0.05% in at least 3 tissues) revealed that 944 (919 upregulated) and 1019 (970 upregulation) BPs are significantly altered in heart 6 and 24 h after infarction, respectively. The results also showed 38 (16 upregulated), 376 (357 upregulated) and 193 (116 upregulated) BPs are significantly altered 24 h after infarction in liver, muscle and adipose, respectively. Most tissues show significant alterations in multiple biological processes, including mitochondrial functions, RNA processes, cell adhesion, ribosome and immune systems. The results of this analysis showed alterations concordant with those observed for KEGG pathways. (B) Reporter metabolites analysis shows significant alteration in important metabolites. Our analysis revealed that 169, 324, 118 and 51 reporter metabolites are significantly altered in heart, liver, skeletal muscle and adipose tissues, respectively, at 24 h post-infarction (Table S4)



E Reg. of transcription from RNAP-II mRNA Processing Regulation of Mitotic Cell Cycle Phase Ubiquitin-dependent Protein Catabolic Process

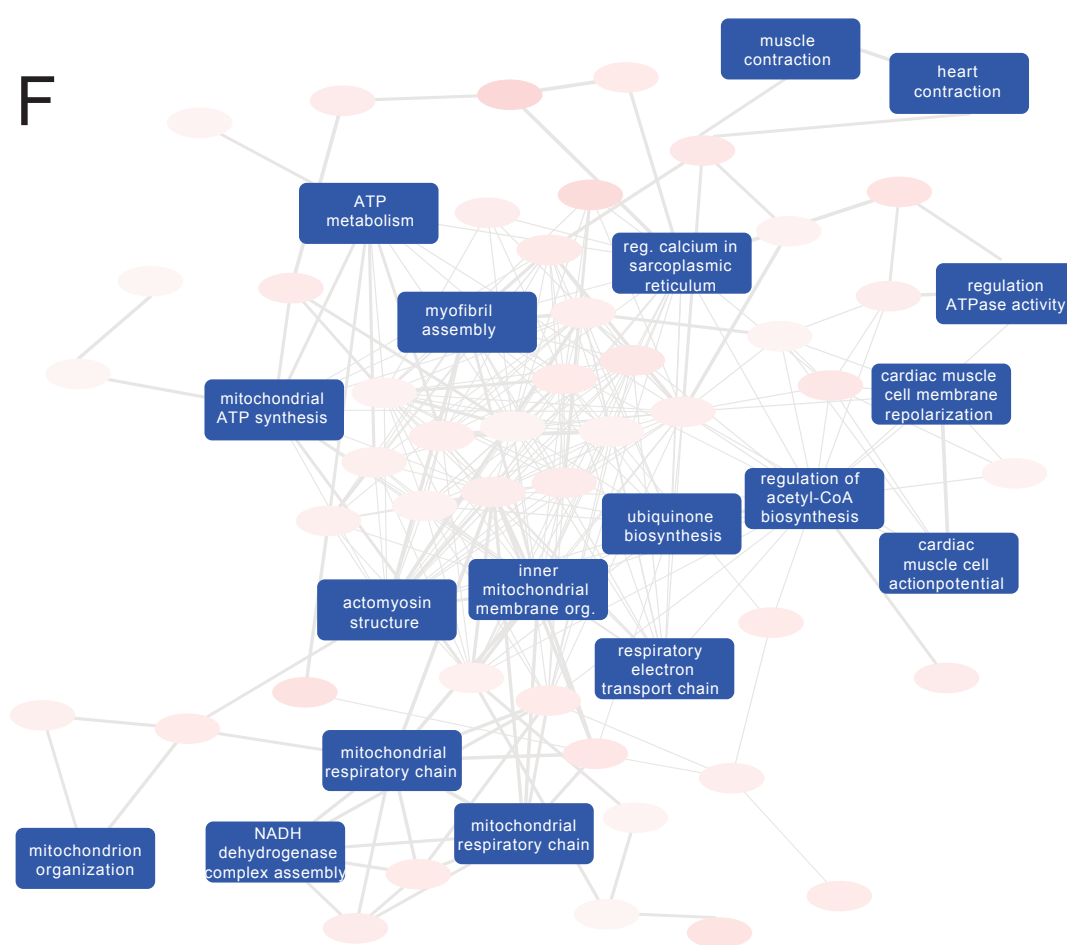
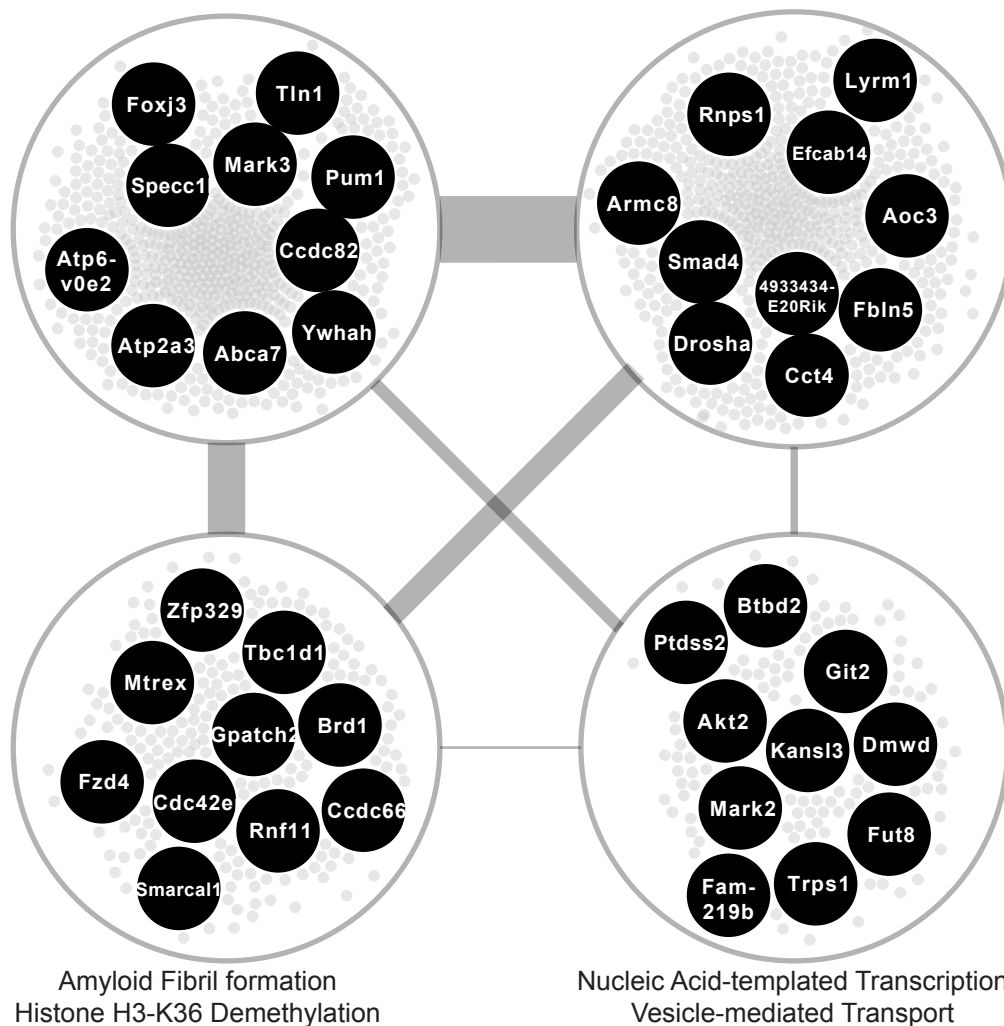


Figure 3 Network analyses. (A) Heart co-expression network clusters with superimposed DEGs 24 h post-infarction (Blue = down-regulated, Red = up-regulated) marked with the cluster numbers. The edges between the clusters were aggregation of the inter-cluster edges (B) Liver. (C) Muscle. (D) Adipose. (E) Intersection of the most central clusters in all tissues shows that the central architecture of the network was conserved in all tissues. We found 4 sub-clusters within the network intersection. Top 10 most connected genes are marked in black. (F) Enriched GO BP in heart-specific cluster generated by Revigo.

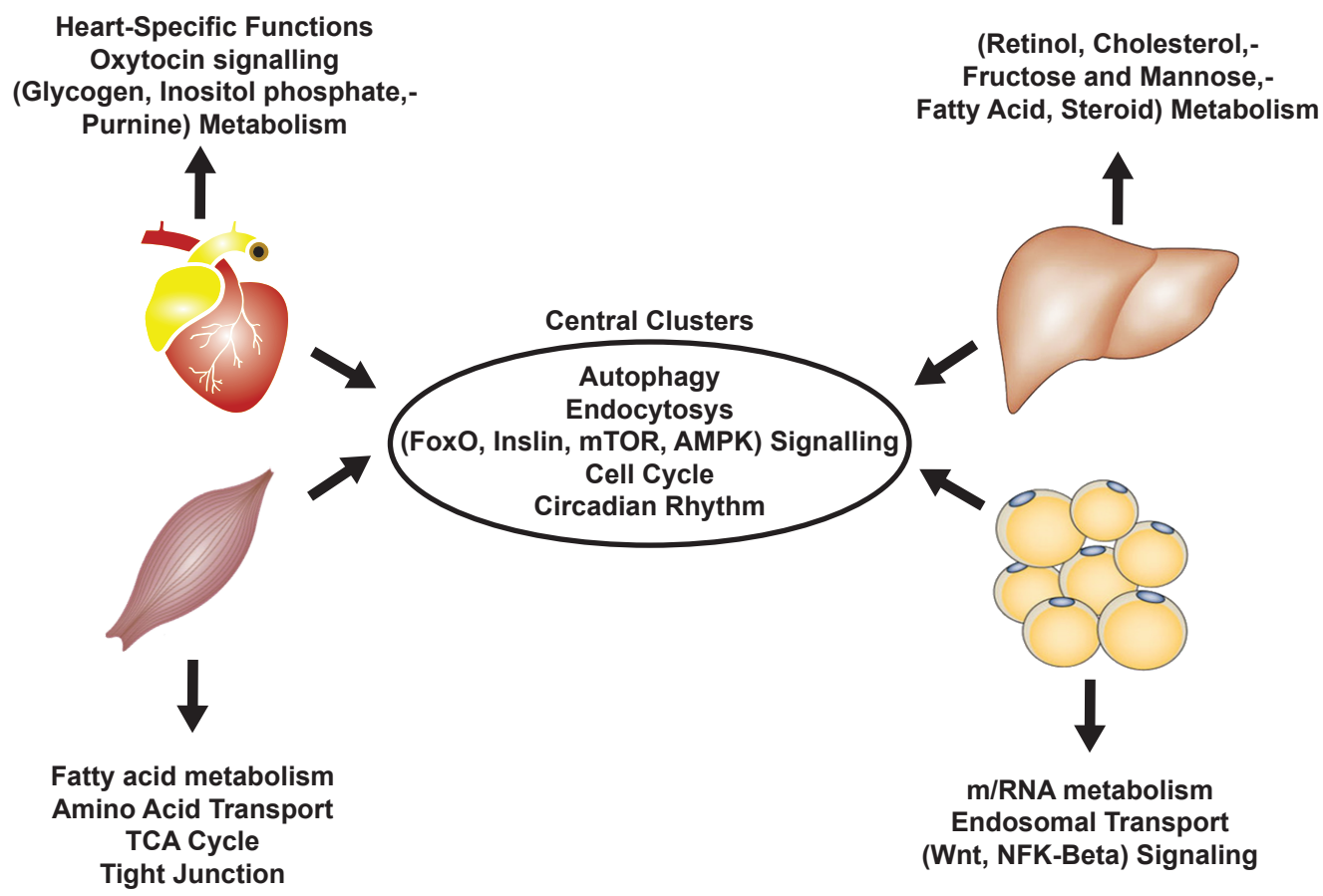
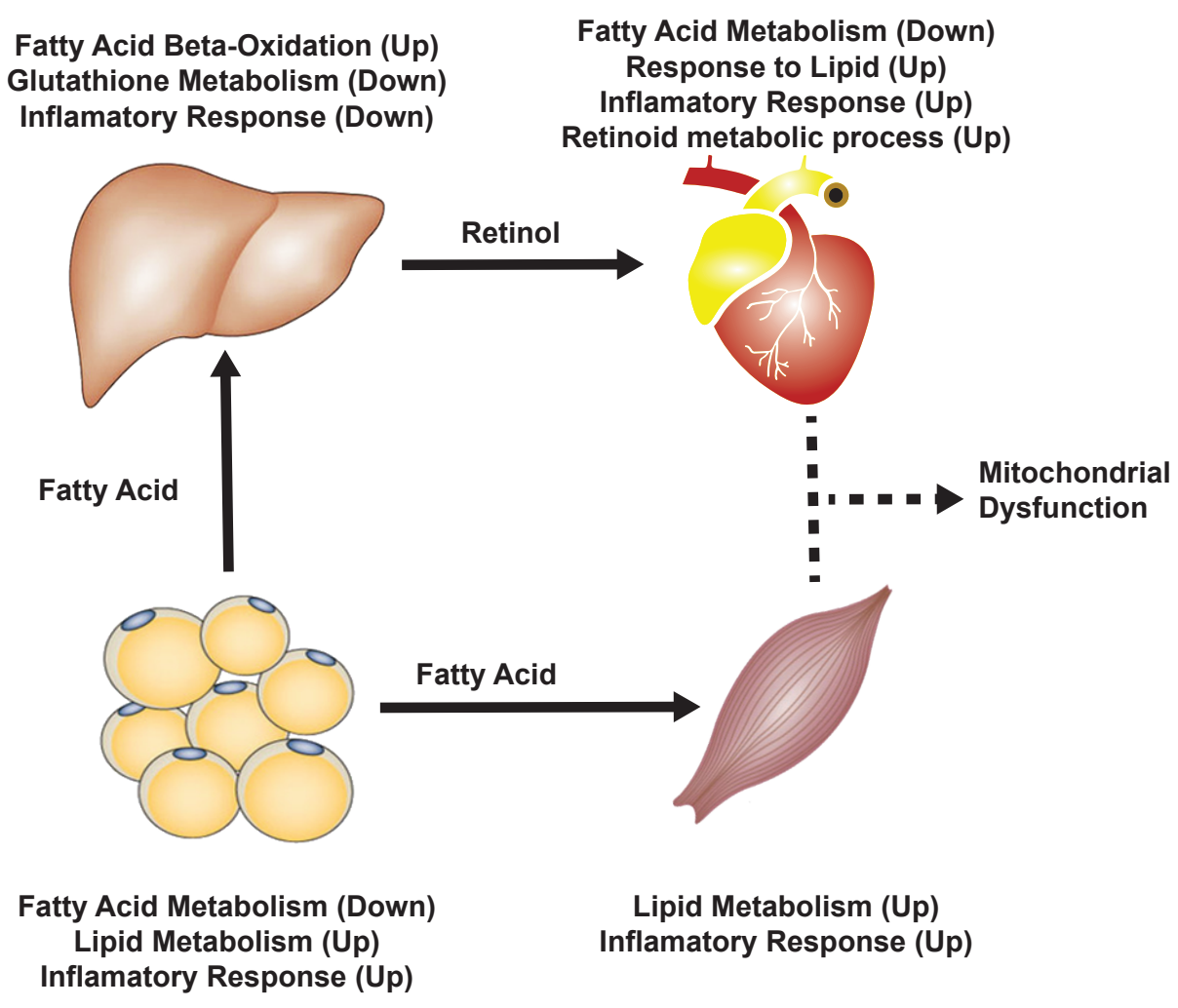
A**B**

Figure 4 (A) Similarity of functions in the most central cluster and specific functions of each tissue-specific cluster. (B) Functional analysis for each tissue and hypothesized flow of metabolites

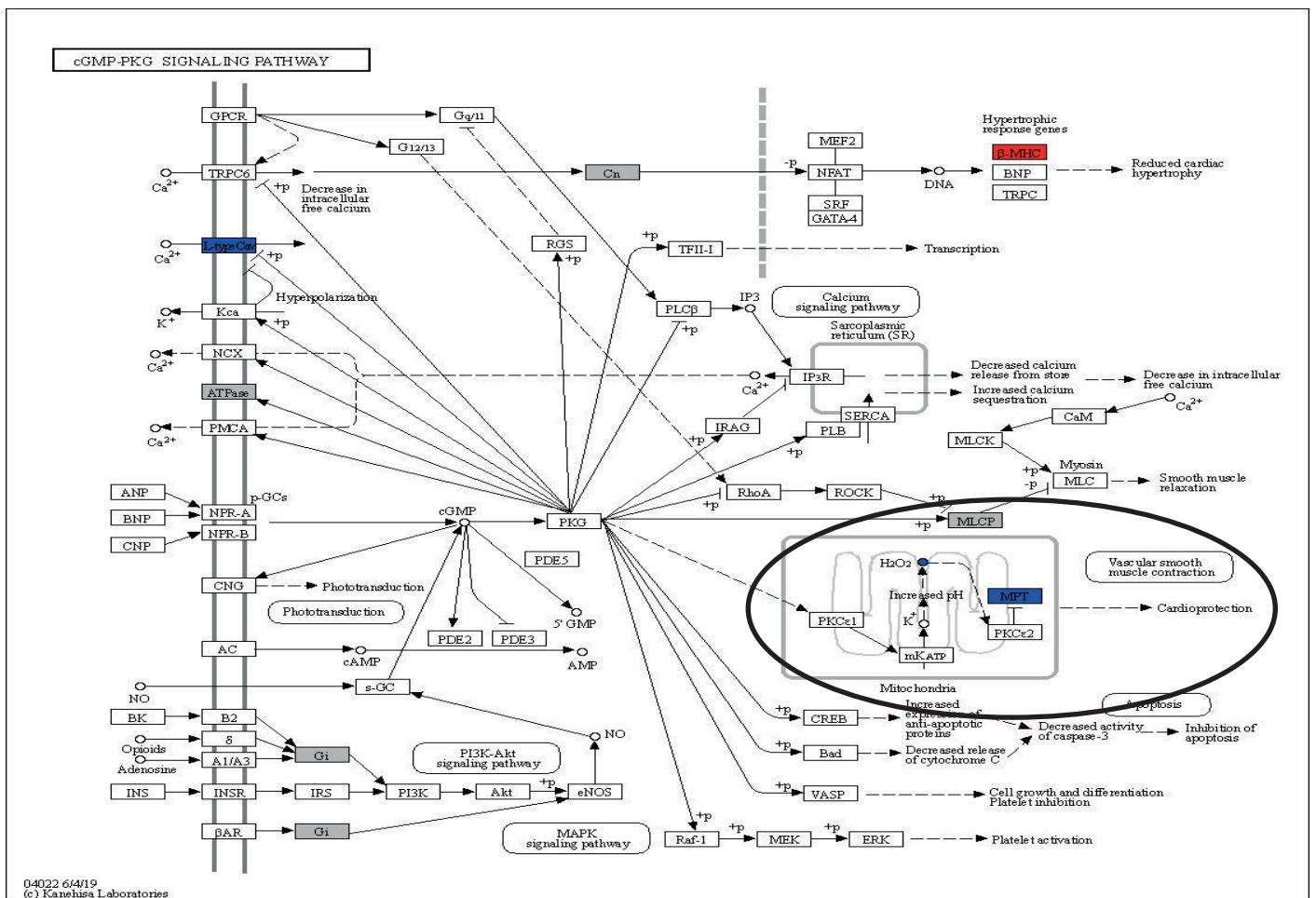


Figure 4 - Figure Supplement 1
cGMP-PKG with overlay data from differential expression and reporter metabolites analysis.

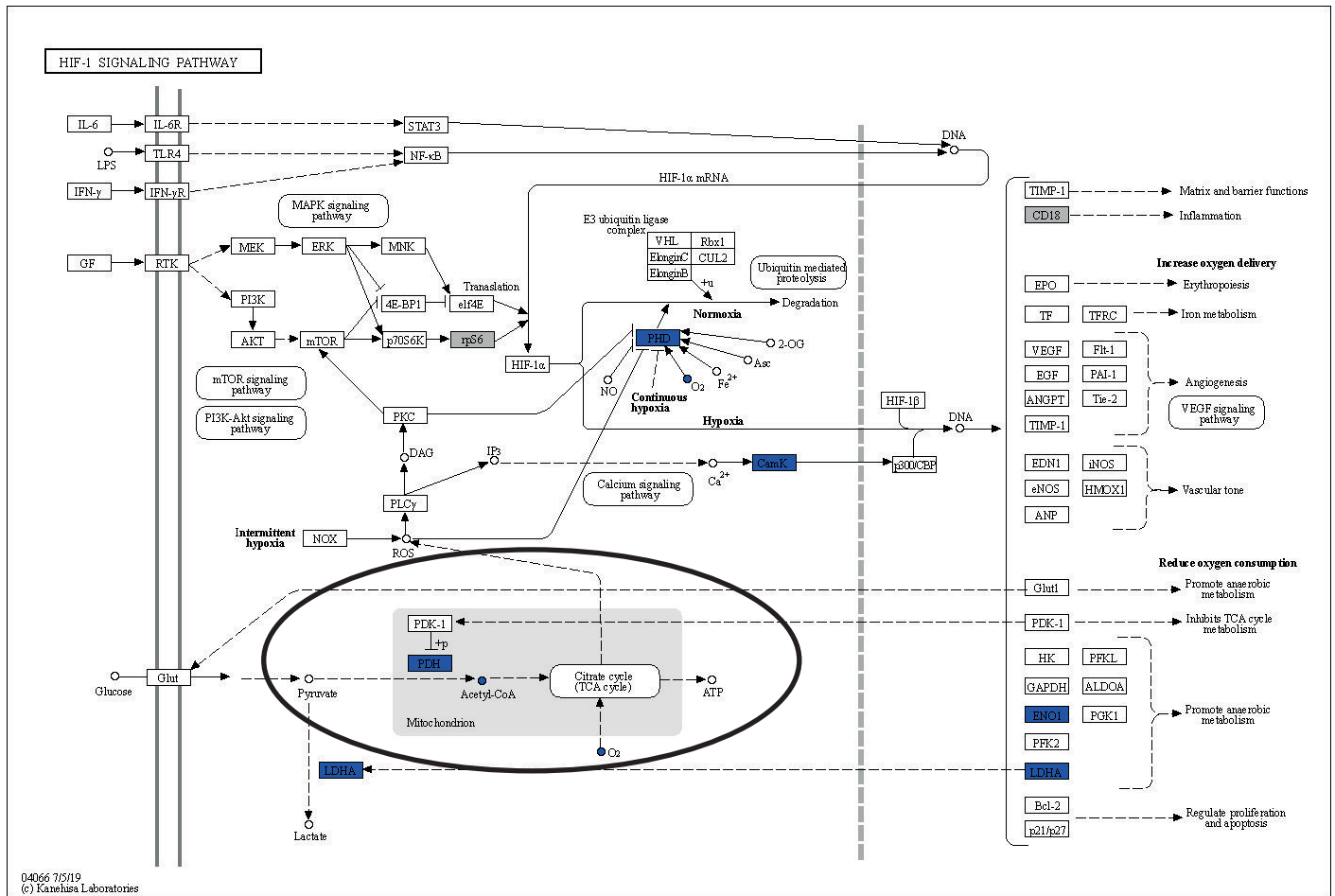


Figure 4 - Figure Supplement 2

HIF-1 signaling pathway with overlay data from differential expression and reporter metabolites analysis.

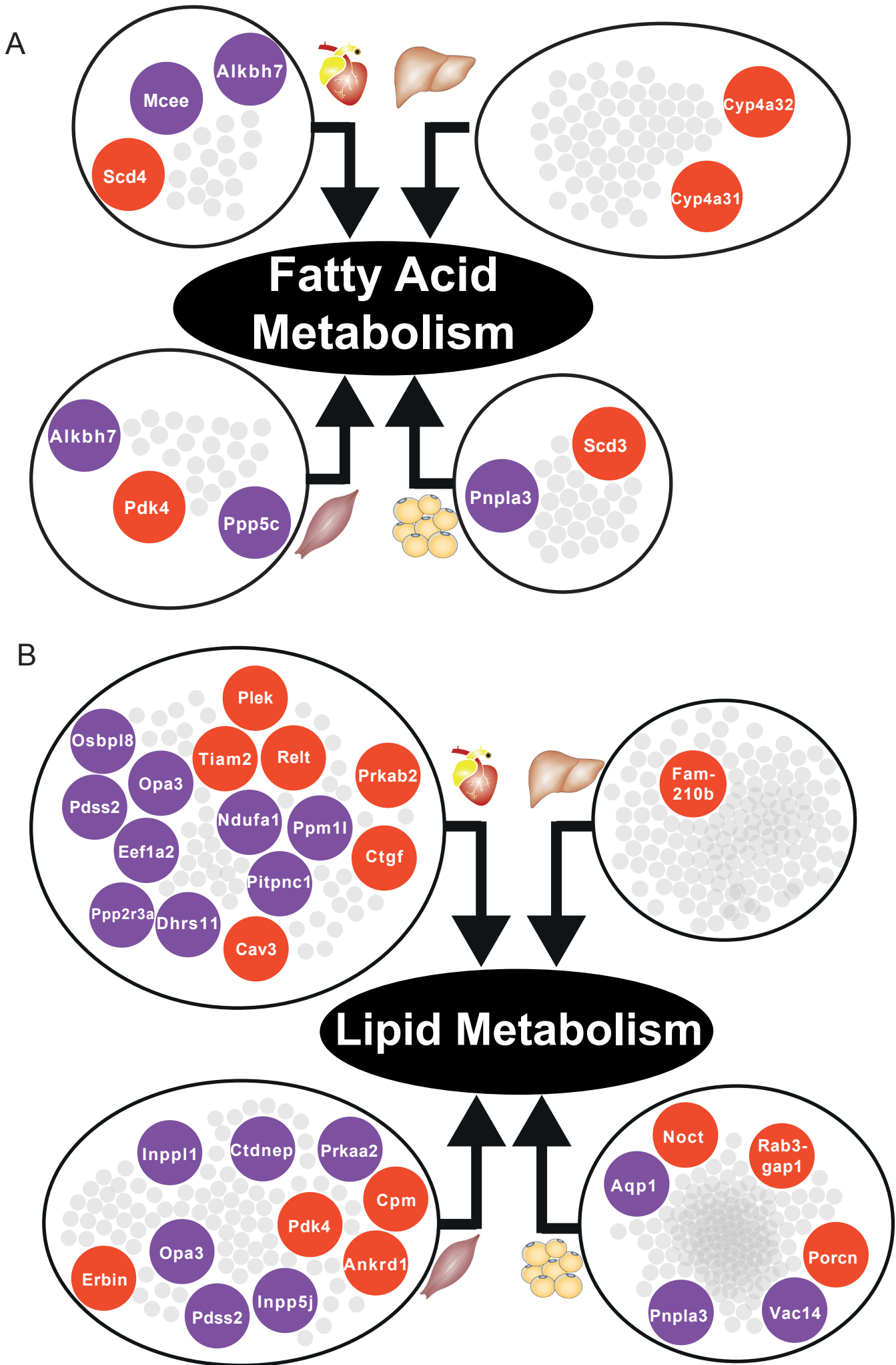


Figure 5 (A) Significantly differentially expressed central genes of each tissue-specific cluster to fatty acid metabolism, as one of the most affected metabolic process. (B) Lipid metabolism. Red = upregulated, blue = downregulated.

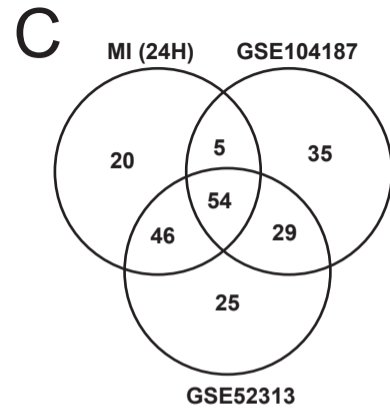
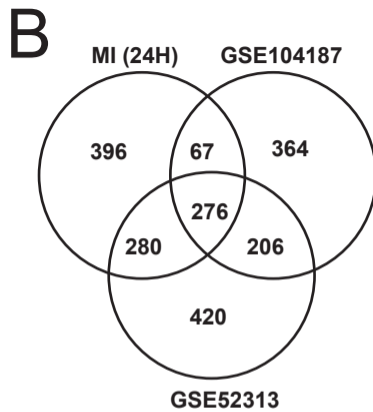
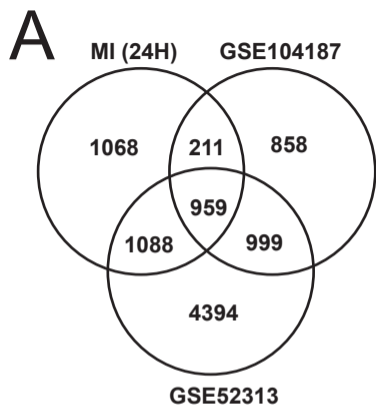


Figure 6 (A) DEGs intersection of our data and validation cohort (B) & (C) Intersection of functional analysis results (GO BP and KEGG Pathways) of our data and validation cohort